Kaon mixing beyond the standard model with physical masses

P. A. Boyle,[1,2] F. Erben [ORCID],[3] J. M. Flynn [ORCID],[4] N. Garron [ORCID],[5,6] J. Kettle,[2] R. Mukherjee [ORCID],[4] and J. T. Tsang [ORCID][3,*]

(RBC and UKQCD Collaborations)

[1]*Brookhaven National Laboratory, Upton, New York 11973, USA*
[2]*Higgs Centre for Theoretical Physics, School of Physics and Astronomy, The University of Edinburgh,*
Edinburgh EH9 3FD, United Kingdom
[3]*CERN, Theoretical Physics Department, Esplanade des Particules 1, 1217 Meyrin, Switzerland*
[4]*School of Physics and Astronomy, University of Southampton, Southampton SO17 1BJ, United Kingdom*
[5]*School of Mathematics, Computer Science and Engineering, Liverpool Hope University,*
Hope Park, Liverpool L16 9JD, United Kingdom
[6]*Theoretical Physics Division, Department of Mathematical Sciences, University of Liverpool,*
Liverpool L69 3BX, United Kingdom

We present nonperturbative results for beyond the standard model kaon mixing matrix elements in the isospin symmetric limit ($m_u = m_d$) of QCD, including a complete estimate of all dominant sources of systematic error. Our results are obtained from numerical simulations of lattice QCD with $N_f = 2 + 1$ flavors of dynamical domain wall fermions. For the first time, these quantities are simulated directly at the physical pion mass $m_\pi \sim 139$ MeV for two different lattice spacings. We include data at three lattice spacings in the range $a = 0.11$–0.07 fm and with pion masses ranging from the physical value up to 450 MeV. Compared to our earlier work, we have added both direct calculations at physical quark masses and a third lattice spacing making the removal of discretization effects significantly more precise and eliminating the need for any significant mass extrapolation beyond the range of simulated data. We renormalize the lattice operators nonperturbatively using RI-SMOM off-shell schemes. These schemes eliminate the need to model and subtract nonperturbative pion poles that arises in the RI-MOM scheme and, since the calculations are performed with domain wall fermions, the unphysical mixing between chirality sectors is suppressed. Our results for the bag parameters in the $\overline{\text{MS}}$ scheme at 3 GeV are $B_K \equiv \mathcal{B}_1 = 0.5240(17)(54)$, $\mathcal{B}_2 = 0.4794(25)(35)$, $\mathcal{B}_3 = 0.746(13)(17)$, $\mathcal{B}_4 = 0.897(02)(10)$ and $\mathcal{B}_5 = 0.6882(78)(94)$, where the first error is from lattice uncertainties and the second is the uncertainty due to the perturbative matching to $\overline{\text{MS}}$.

I. INTRODUCTION

A. Standard model kaon mixing

Neutral kaon mixing has long been an important area of study in standard model (SM) particle physics. Most famously, *CP* violation was first observed in the Nobel-prize-winning Christenson-Cronin-Fitch-Turlay experiment [1]. Interested readers are referred to Refs. [2–4] and references therein. Kaon mixing is mediated by a flavor changing neutral current interaction, which is absent at tree-level, whereby the neutral kaon oscillates with its anti-particle. The leading-order SM processes are the well-known *W* exchange box diagrams shown in Fig. 1.

Typically, one separates the short and long distance contribution to this process using the operator product expansion (OPE). This isolates the nonperturbative matrix element which can be computed using lattice QCD, $\langle \bar{K}^0 | O_1 | K^0 \rangle$, of the (vector–axial) × (vector–axial) four-quark left handed operator O_1 from the perturbatively computed Inami-Lim functions [5]. Conventionally, the hadronic contribution to the matrix element is parametrized by the kaon bag parameter and has been the subject of many lattice calculations [6–12]. It is now known at the percent-level and is reported in the FLAG [13] review with consistent results from multiple collaborations.
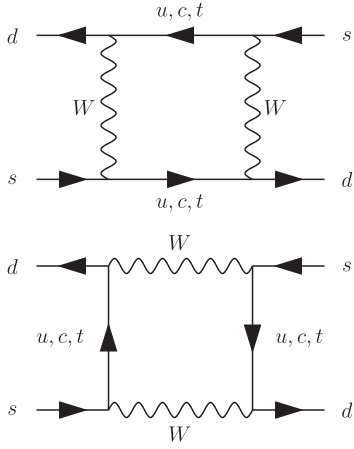
FIG. 1. *W* exchange box diagrams mediating neutral kaon mixing in the standard model.

The SM operator matrix element is a factor in the expression for the dominant short-distance contribution to the indirect CP-violation parameter ε_K. Lattice computations of the matrix element have reached the point where isospin and electromagnetic effects are as large as the total error quoted in the isospin-symmetric pure QCD theory. However, including these effects would need to be accompanied by reduced uncertainty in the Cabibbo-Kobayashi-Maskawa (CKM) quark-mixing matrix element $|V_{cb}|$, also appearing in the SM short-distance contribution to ε_K [13,14].

For greater precision in the short-distance contribution to be meaningful, we would in addition need to include long-distance effects from bilocal V–A currents where two weak Hamilton insertions are connected by quark loops. Initial progress has been made in Refs. [15–17]. The precision on the computation of ΔM_K, including all long-distance effects, is already at the 10% level [18]. A first full computation of the long-distance part of ε_K at the level of 40% precision has recently been reported in Ref. [19]. For recent broader reviews of the status and prospects of kaon physics we refer the interested reader to Refs. [20–22].

B. Beyond the standard model kaon mixing

Beyond the standard model (BSM), new mediating particles could contribute to neutral kaon mixing. These mediators are not restricted to the V–A Dirac structure of the *W* boson and new four-quark operators would be allowed in the effective Hamiltonian with Wilson coefficients suppressed by the new mass scale. Eight such four-quark operators are allowed, but for computing their $K^0 \bar{K}^0$ matrix elements only five parity-even operators are needed, shown in Eq. (2.3), which are model independent and whose hadronic matrix elements can be calculated using lattice QCD. Any BSM contributions to the V–A structure would be very hard to distinguish from the SM signal in experiments. However the new color-Dirac structure operators have no SM contribution at this order in the weak

forces and thus new physics arising from these operators would be easier to detect in experiment. In addition, the matrix elements of these BSM operators are enhanced in the chiral limit compared to the SM operator, as can be seen from their chiral expansions. Therefore our results can be combined with the experimental value of ε_K to constrain the parameter space of specific BSM theories and the scale of new physics, see for example Ref. [23].

Lattice QCD appears as a natural candidate for computing the BSM operator matrix elements. However the mixing pattern of these four-quark operators makes this more challenging than the computation for B_K alone. We refer the interested reader to the pedagogical review [24]. Here we take advantage of the good chiral-flavor properties of the domain wall fermion formulation to constrain the mixing to be the same as in the continuum theory. In practice, this is only true up to lattice artefacts that are exponentially suppressed in the extent of the domain wall fifth dimension and that we must keep under control.

Early studies of BSM kaon mixing [25–27] were performed in the quenched approximation. They were followed by dynamical simulations with N_f quark flavors by several collaborations: RBC-UKQCD $(N_f = 2 + 1)$ [28,29], SWME $(N_f = 2 + 1)$ [8,9,30], and ETM $(N_f = 2)$ [12] and $(N_f = 2 + 1 + 1)$ [11]. In contrast to results for the SM operator, there are tensions between the different collaborations' results for some of the BSM operators, as shown in Table I—in which we already anticipate the results of this work—and summarized in the FLAG report [13]. We note that a similar discrepancy is observed in neutral $B_{(s)}$-mixing [13,31].

In Refs. [29,33], it was proposed that the source of these tensions was the choice of the intermediate renormalization scheme. Specifically, it was proposed that the symmetric momentum subtraction scheme RI-SMOM (which has nonexceptional kinematics) advocated by RBC-UKQCD has several beneficial features compared to the previously used RI-MOM (which has exceptional kinematics). This is likely due to the exceptional (divergent in the massless limit), infrared nonperturbative "pion pole" behavior in the RI-MOM vertex functions, which must be correctly modeled and subtracted, while the mass is simultaneously taken to zero to establish a mass independent scheme. This behavior is absent in the RI-SMOM scheme, giving greater theoretical control as it avoids the possibility of imperfect modelling of the nonperturbative pole systematically affecting the result. The results obtained from two RI-SMOM schemes are in agreement with each other and with the perturbatively renormalized results from the SWME collaboration [8,9,30], while the calculation with RI-MOM agreed with previous RBC-UKQCD [28] and ETM [11,12] results which also used RI-MOM.

This paper improves upon our most recent RBC-UKQCD BSM kaon mixing calculation [29,33] by adding a third lattice spacing and including two data points at the

TABLE I. Results from calculations of BSM bag parameters in $\overline{\mathrm{MS}}(\mu = 3 \text{ GeV})$ from RBC-UKQCD, SWME and ETM show tensions for $\mathcal{B}_4$ and $\mathcal{B}_5$. The results obtained by ETM, which were renormalized via RI-MOM, agree with RBC-UKQCD's results obtained via RI-MOM. The SWME results, obtained via a 1 loop intermediate scheme agree with RBC-UKQCD's results obtained via RI-SMOM, for both γ_μ and $\not{q}$ [32]. This suggests tensions arise from the implementation of intermediate schemes, in particular caused by RI-MOM exhibiting exceptional infrared behavior which is absent in RI-SMOM. All results are shown in the SUSY basis.

	ETM12 [12]	ETM15 [11]	RBC-UKQCD12 [28]	SWME15 [9]	RBC-UKQCD16 [29]		THIS WORK
N_f	2	$2+1+1$	$2+1$	$2+1$	$2+1$	$2+1$	$2+1$
Scheme	RI-MOM	RI-MOM	RI-MOM	1 loop	RI-SMOM	RI-MOM	RI-SMOM
$\mathcal{B}_2$	0.47(2)	0.46(3)(1)	0.43(5)	0.525(1)(23)	0.488(7)(17)	0.417(6)(2)	0.4794(25)(35)
$\mathcal{B}_3$	0.78(4)	0.79(5)(1)	0.75(9)	0.773(6)(35)	0.743(14)(65)	0.655(12)(44)	0.746(13)(17)
$\mathcal{B}_4$	0.76(3)	0.78(4)(3)	0.69(7)	0.981(3)(62)	0.920(12)(16)	0.745(9)(28)	0.897(02)(10)
$\mathcal{B}_5$	0.58(3)	0.49(4)(1)	0.47(6)	0.751(7)(68)	0.707(8)(44)	0.555(6)(53)	0.6882(78)(94)

physical light quark mass. We present results in the isospin symmetric limit of pure $N_f = 2 + 1$ QCD with sufficient precision that further work on this topic must address the strong and electromagnetic isospin breaking effects. The status of this work has been previously reported in Refs. [34,35]. Finally, it is worth noting that a similar analysis performed in the pion sector allows to extract the matrix elements which could dominate the short-distance contribution to neutrinoless double beta decays, see for example Refs. [36,37]. In particular, the renormalization factors computed here could be employed for such a study.

II. BACKGROUND

A. Effective weak Hamiltonian and BSM basis

By integrating out heavy particles such as the W boson we can separate the long- and short-distance effects into matrix elements, $\langle \bar{K}^0 | O_i | K^0 \rangle$, and Wilson coefficients respectively. Beyond the standard model a generic effective weak $\Delta S = 2$ Hamiltonian can be constructed, in which the standard model operator, O_1 below, and seven additional four-quark operators appear

$$\mathcal{H}^{\Delta S=2} = \sum_{i=1}^{5} C_i(\mu) O_i(\mu) + \sum_{i=1}^{3} \widetilde{C}_i(\mu) \widetilde{O}_i(\mu), \quad (2.1)$$

where μ is a renormalisation scale. The Wilson coefficients $C_i(\mu)$ depend on the BSM physics, but the QCD matrix elements $\langle \overline{K}^0 | O_i | K^0 \rangle$ do not. The operators O_i in the so-called "SUSY basis" introduced in Ref. [38] are

$$O_1 = \bar{s}_a \gamma_\mu (1 - \gamma_5) d_a \bar{s}_b \gamma_\mu (1 - \gamma_5) d_b,$$
$$O_2 = \bar{s}_a (1 - \gamma_5) d_a \bar{s}_b (1 - \gamma_5) d_b,$$
$$O_3 = \bar{s}_a (1 - \gamma_5) d_b \bar{s}_b (1 - \gamma_5) d_a,$$
$$O_4 = \bar{s}_a (1 - \gamma_5) d_a \bar{s}_b (1 + \gamma_5) d_b,$$
$$O_5 = \bar{s}_a (1 - \gamma_5) d_b \bar{s}_b (1 + \gamma_5) d_a, \quad (2.2)$$

where a, b are color indices. The $\widetilde{O}_{1,2,3}$ are parity partners of $O_{1,2,3}$ obtained by swapping $1 - \gamma_5 \rightarrow 1 + \gamma_5$, while $O_{4,5}$ are parity-even. Owing to parity invariance of QCD, only the parity even parts, denoted with a $+$ superscript, contribute in the $\langle \bar{K}^0 | O_i | K^0 \rangle$ matrix elements

$$O_1^+ = \bar{s}_a \gamma_\mu d_a \bar{s}_b \gamma_\mu d_b + \bar{s}_a \gamma_\mu \gamma_5 d_a \bar{s}_b \gamma_\mu \gamma_5 d_b,$$
$$O_2^+ = \bar{s}_a d_a \bar{s}_b d_b + \bar{s}_a \gamma_5 d_a \bar{s}_b \gamma_5 d_b,$$
$$O_3^+ = \bar{s}_a d_b \bar{s}_b d_a + \bar{s}_a \gamma_5 d_b \bar{s}_b \gamma_5 d_a,$$
$$O_4^+ = \bar{s}_a d_a \bar{s}_b d_b - \bar{s}_a \gamma_5 d_a \bar{s}_b \gamma_5 d_b,$$
$$O_5^+ = \bar{s}_a d_b \bar{s}_b d_a - \bar{s}_a \gamma_5 d_b \bar{s}_b \gamma_5 d_a. \quad (2.3)$$

In practice we find it convenient to work in a different basis, referred to as the "lattice" or "NPR" basis [33]. This comprises color-unmixed operators obtained by Fierz transforming the equivalent color-mixed operators, as detailed in Appendix D, with $Q_1 = O_1$ and

$$Q_2 = \bar{s}_a \gamma_\mu (1 - \gamma_5) d_a \bar{s}_b \gamma_\mu (1 + \gamma_5) d_b,$$
$$Q_3 = \bar{s}_a (1 - \gamma_5) d_a \bar{s}_b (1 + \gamma_5) d_b,$$
$$Q_4 = \bar{s}_a (1 - \gamma_5) d_a \bar{s}_b (1 - \gamma_5) d_b,$$
$$Q_5 = \frac{1}{4} \bar{s}_a \sigma_{\mu\nu} (1 - \gamma_5) d_a \bar{s}_b \sigma_{\mu\nu} (1 + \gamma_5) d_b. \quad (2.4)$$

Again we need to consider only the parity-conserving parts which read

$$Q_1^+ = \bar{s}_a \gamma_\mu d_a \bar{s}_b \gamma_\mu d_b + \bar{s}_a \gamma_\mu \gamma_5 d_a \bar{s}_b \gamma_\mu \gamma_5 d_b,$$
$$Q_2^+ = \bar{s}_a \gamma_\mu d_a \bar{s}_b \gamma_\mu d_b - \bar{s}_a \gamma_\mu \gamma_5 d_a \bar{s}_b \gamma_\mu \gamma_5 d_b,$$
$$Q_3^+ = \bar{s}_a d_a \bar{s}_b d_b - \bar{s}_a \gamma_5 d_a \bar{s}_b \gamma_5 d_b,$$
$$Q_4^+ = \bar{s}_a d_a \bar{s}_b d_b + \bar{s}_a \gamma_5 d_a \bar{s}_b \gamma_5 d_b,$$
$$Q_5^+ = \sum_{\nu > \mu} \bar{s}_a \gamma_\mu \gamma_\nu d_a \bar{s}_b \gamma_\mu \gamma_\nu d_b. \quad (2.5)$$

We perform the lattice calculations and renormalization in this basis and transform to the SUSY basis prior to performing the required chiral and continuum limit extrapolations.[1] Observe that under $SU(3)_L \times SU(3)_R$ quark flavor symmetry, $O_1^{(+)}$ transforms as $(27, 1)$, $O_{2,3}^{(+)}$ as $(6, \bar{6})$ and $O_{4,5}^{(+)}$ as $(8, 8)$, while $Q_1^{(+)}$ is $(27, 1)$, $Q_{2,3}^{(+)}$ are $(8, 8)$ and $Q_{4,5}^{(+)}$ are $(6, \bar{6})$.

B. Bag parameters

The conventional way to parameterise the hadronic matrix elements of the four-quark operators is through the so-called bag parameters, defined as the ratio of the matrix elements over their vacuum saturation approximation (VSA) value

$$\mathcal{B}_i(\mu) = \frac{\langle \bar{K}^0 | O_i(\mu) | K^0 \rangle}{\langle \bar{K}^0 | O_i(\mu) | K^0 \rangle_{\text{VSA}}}. \tag{2.6}$$

For the standard model operator, $B_K \equiv \mathcal{B}_1$ is given by,

$$\mathcal{B}_1(\mu) = \frac{\langle \bar{K}^0 | O_1(\mu) | K^0 \rangle}{\frac{8}{3} m_K^2 f_K^2}, \tag{2.7}$$

where m_K is the mass of the kaon and f_K is the kaon decay constant defined by the coupling of the kaon to the renormalized axial-vector current $\mathbb{A}_\mu^R$,

$$\langle 0 | \mathbb{A}_\mu^R(x) | K(p) \rangle = i f_K p_\mu e^{-ip \cdot x}, \tag{2.8}$$

where p_μ is the 4-momentum of the kaon. The BSM bag parameters are,

$$\mathcal{B}_i(\mu) = \frac{(m_s(\mu) + m_d(\mu))^2}{N_i m_K^4 f_K^2} \langle \bar{K}^0 | O_i(\mu) | K^0 \rangle, \quad i > 1, \tag{2.9}$$

and the factors N_i in the SUSY basis are $N_{i>1}^{\text{SUSY}} = -\frac{5}{3}, \frac{1}{3}, 2, \frac{2}{3}$. The corresponding factors in the parity-even NPR basis are $N_{i>1}^{\text{NPR}} = -\frac{4}{3}, 2, -\frac{5}{3}, -1$. The VSA replaces the four-quark matrix elements with products of two-quark matrix elements. When "chirally enhanced" matrix elements of the pseudoscalar density $\bar{s}\gamma_5 d$ appear, matrix elements of axial vector and tensor currents are dropped. This leads to the appearance of the square of the ratio $(m_s(\mu) + m_d(\mu))/m_K^2 f_K$ in the $\mathcal{B}_i$ for $i > 1$.

C. Ratios R_i of BSM to SM matrix elements

The bag parameters are not the only way to parametrize these four-quark operators; other quantities have been defined, for example in Refs. [26,27,39]. Here we choose

to consider the simple ratios of the BSM to SM matrix elements

$$R_i(\mu) = \frac{\langle \bar{P} | O_i(\mu) | P \rangle}{\langle \bar{P} | O_1(\mu) | P \rangle}, \quad i = 2, \ldots, 5. \tag{2.10}$$

There are some clear advantages: there is no explicit quark-mass dependence in the expression, so that the BSM matrix elements can be recovered from knowledge of R_i, the SM bag parameter $\mathcal{B}_1$ and the experimentally measured kaon mass and decay constant [cf. Eq. (2.7)]. Additionally, the similarity of the numerator and denominator leads to partial cancellation of systematic and statistical errors. Another approach originally proposed in Ref. [40] is to consider quantities in which the chiral logs cancel out (either at all orders or at NLO). This strategy has been employed for example in Refs. [11,29,39].

III. SIMULATION DETAILS AND ENSEMBLE PROPERTIES

A. Simulation parameters

We use RBC-UKQCD's $N_f = 2 + 1$ gauge ensembles [6,7,32,41–43] generated with the Iwasaki gauge action [44,45] and a domain wall fermion (DWF) action with either Möbius (M) [46–48] or Shamir (S) [49] kernel. In our work the Möbius and Shamir kernels differ only in their approximation of the sign function, and agree in the limit $L_s \to \infty$, where L_s is the size of the fifth dimension [7]. We hence assume that the Möbius and Shamir kernels lie on the same scaling trajectory. The set of ensembles contains three lattice spacings in the range $a = 0.11$–0.07 fm, labeled C(oarse), M(edium) and F(ine), and includes two physical pion mass ensembles. The remaining ensembles have heavier pion masses ranging up to $m_\pi \approx 450$ MeV, which are used to guide the small chiral extrapolation on the finest ensemble.

On each ensemble, the light valence-quark mass (am_l^{uni}) was chosen identical to the light-quark mass in the sea. The strange valence quark mass (am_s^{val}) was simulated near its physical value (am_s^{phys}) which typically differs from the sea quark mass (am_s^{sea}). The main ensemble properties and the simulated masses are listed in Table II. Large parts of the data were generated using the grid and hadrons framework [50–52].

The lattice scale and the physical light and strange quark masses were set using the physical values of m_π, m_K and m_Ω [7] before the ensemble F1M was generated. This fit was repeated including the ensemble F1M in Ref. [43] where more details about this ensemble are described. We also introduce two new ensembles "C1M" and "M1M," which are the Möbius equivalents of the C1S and M1S. Since they share the same gauge coupling and Möbius scale as the C0M and M0M, respectively, they have the same lattice spacing and physical strange quark mass.

---

[1]Unless stated otherwise all results in this paper are quoted in the SUSY basis.

TABLE II.   Summary of the main parameters of the ensembles used in this work. In the ensemble name the first letter (C, M or F) stand for coarse, medium and fine, respectively. The last letter (M or S) stands for Möbius and Shamir kernels, respectively. The column N_{conf} denotes the number of de-correlated gauge field configurations, N_{src} the number of equivalent measurements per configuration.

Name	L/a	T/a	a^{-1} [GeV]	m_π [MeV]	$N_{\text{conf}} \times N_{\text{src}}$	am_l^{uni}	am_s^{sea}	am_s^{val}	am_s^{phys}
C0M	48	96	1.7295(38)	139	90×48	0.00078	0.0362	0.0358	0.03580(16)
C1S	24	64	1.7848(50)	340	100×32	0.005	0.04	0.03224	0.03224(18)
C2S	24	64	1.7848(50)	431	99×32	0.01	0.04	0.03224	0.03224(18)
M0M	64	128	2.3586(70)	139	82×64	0.000678	0.02661	0.0254	0.02539(17)
M1S	32	64	2.3833(86)	304	83×32	0.004	0.03	0.02477	0.02477(18)
M2S	32	64	2.3833(86)	361	76×32	0.006	0.03	0.02477	0.02477(18)
M3S	32	64	2.3833(86)	411	80×32	0.008	0.03	0.02477	0.02477(18)
F1M	48	96	2.708(10)	232	72×48	0.002144	0.02144	0.02144	0.02217(16)
C1M[a]	24	64	1.7295(38)	276	$\cdots$	0.005	0.0362	$\cdots$	0.03580(16)
M1M[a]	32	64	2.3586(70)	286	$\cdots$	0.004	0.02661	$\cdots$	0.02539(17)

[a]These ensembles only enter the analysis in order to constrain the chiral extrapolation of the renormalization constants described in Sec. IV.

More details about these ensembles are summarized in Appendix A.

B. Correlation functions

The quark propagators $S_F(y, x)$, where we write $x = (\mathbf{x}, t_x)$, are obtained by inverting the domain wall Dirac operators on $\mathbb{Z}_2$ noise wall sources $\eta(x)$ [53–55]. In order to improve the overlap with the ground state, these sources are Gaussian-smeared following a Jacobi procedure, i.e.

$$\eta_\omega(\mathbf{x}, t_{\text{src}}) = \sum_{\mathbf{y}} \omega_{\text{src}}^S(\mathbf{x}, \mathbf{y})\eta(\mathbf{y}, t_y)\delta_{t_y, t_{\text{src}}}, \quad (3.1)$$

where we omit spin-color indices for simplicity. Further details about the smearing parameters defining ω can be found in Ref. [43].

At the sink, we consider both the local (L) and smeared (S) case,

$$S_F^{L,S}(x, y) = \sum_{\mathbf{z}} \omega_{\text{snk}}^{L,S}(\mathbf{x}, \mathbf{z})S(z, y)\delta_{t_x, t_z}, \quad (3.2)$$

where $\omega^L(\mathbf{x}, \mathbf{y}) = \delta_{\mathbf{x}, \mathbf{y}}$. From these propagators, we construct two-point functions which are defined by

$$C_{\Gamma_1, \Gamma_2}^{s_1, s_2}(t) \equiv \sum_{\mathbf{x}} \langle (O_{\Gamma_2}^{s_2}(\mathbf{x}, t))(O_{\Gamma_1}^{s_1}(\mathbf{0}, 0))^\dagger \rangle$$
$$= \sum_n \frac{(M_{\Gamma_2}^{s_2})_n (M_{\Gamma_1}^{s_1})_n^*}{2E_n}(e^{-E_n t} \pm e^{-E_n(T-t)}), \quad (3.3)$$

where O_Γ^s is a bilinear with the flavor content of a kaon, defined by

$$O_\Gamma^s(\mathbf{x}, t) = \left(\bar{q}_2(\mathbf{x}, t)\sum_{\mathbf{y}}\omega_s(\mathbf{x}, \mathbf{y})\Gamma q_1(\mathbf{y}, t)\right). \quad (3.4)$$

The Dirac structure is represented by Γ_i. The hadronic matrix elements are denoted by $(M_\Gamma^s)_n = \langle X_n|(O_\Gamma^s)^\dagger|0\rangle$ (so that $(\bar{M}_\Gamma^s)_n = (M_\Gamma^s)_n^* = \langle 0|O_\Gamma^s|X_n\rangle$) with the nth excited meson states $|X_n\rangle$ with corresponding energy E_n. For the bilinear, we only consider pseudoscalars ($\Gamma = \gamma_5 \equiv P$) and the temporal component of the axial current ($\Gamma = \gamma_0\gamma_5 \equiv A$). The smearing operator ω_s and the superscripts s_1, s_2 label the type of smearing. In our setup, we use local (L) and smeared (S) propagators at source and sink. At the source, all our quark fields are smeared, $s_1 = SS$. We also require the smearing at the sink to be the same for both the strange and the down quark, $s_2 \in \{SS, LL\}$. An exception to this is the ensemble F1M, where we keep both the source and sink local, $s_1 = s_2 = LL$.

For three-point correlation functions, in contrast to the two-point functions, we consider only pseudoscalar operators $\bar{\mathbb{P}}$ ($\mathbb{P}$) inducing the quantum numbers of a $\bar{K}$ (K) at the source (sink). These operators are smeared ($s = SS$) on all ensembles apart from the F1M, where they are local ($s = LL$). For notational convenience we drop the smearing indices for the operators. Dropping around-the-world effects, we obtain

$$C_3^i(t, \Delta T)$$
$$\equiv \langle \mathbb{P}(\Delta T)Q_i^+(t)\bar{\mathbb{P}}^\dagger(0)\rangle$$
$$= \sum_{n,n'} \frac{(M_P^s)_n}{4E_n E_{n'}} \langle X_n|Q_i^+(t)|X_{n'}\rangle (M_P^s)_{n'}^* e^{-(\Delta T-t)E_n} e^{-tE_{n'}}.$$

$$(3.5)$$

TABLE III. Bare bag parameters on all ensembles quoted in the NPR basis.

$N_i \mathcal{B}_i^{\text{bare}}\|_{\text{NPR}}$	$i = 1$	$i = 2$	$i = 3$	$i = 4$	$i = 5$
C0M	1.5565(17)	−1.22385(96)	1.8631(15)	−0.96015(86)	−0.49446(43)
C1S	1.5692(28)	−1.2294(18)	1.8574(27)	−0.9907(17)	−0.51051(86)
C2S	1.5949(24)	−1.2366(16)	1.8586(23)	−1.0118(15)	−0.52241(74)
M0M	1.4890(21)	−1.2052(11)	1.8461(17)	−0.87841(86)	−0.44361(42)
M1S	1.5038(35)	−1.2066(26)	1.8374(41)	−0.9051(23)	−0.4577(11)
M2S	1.5101(24)	−1.2119(20)	1.8409(31)	−0.9133(17)	−0.46219(80)
M3S	1.5223(45)	−1.2129(30)	1.8380(47)	−0.9252(26)	−0.4684(13)
F1M	1.4776(34)	−1.1901(20)	1.8218(30)	−0.8691(14)	−0.43601(70)

TABLE IV. Bare ratio parameters on all ensembles quoted in the NPR basis.

$R_i^{\text{bare}}\|_{\text{NPR}}$	$i = 2$	$i = 3$	$i = 4$	$i = 5$
C0M	−23.511(30)	35.788(48)	−18.439(28)	−9.494(15)
C1S	−20.587(55)	31.098(85)	−16.592(59)	−8.549(31)
C2S	−18.368(35)	27.604(56)	−15.001(43)	−7.747(23)
M0M	−28.144(39)	43.113(60)	−20.516(29)	−10.361(15)
M1S	−25.125(72)	38.25(11)	−18.848(72)	−9.531(36)
M2S	−23.505(51)	35.704(81)	−17.742(67)	−8.979(33)
M3S	−22.107(56)	33.501(88)	−16.866(65)	−8.538(33)
F1M	−28.621(80)	43.82(13)	−20.929(70)	−10.500(36)

$C_3^i(t, \Delta T)$ describes a three-point correlation function with a source at $t = 0$, sink at $t = \Delta T$ and a four-quark operator insertion Q_i^+ at t.

By placing sources on every second time plane, we compute the above correlation functions for $(T/a)/2$ time translations, where T/a is the integer number of time slices for a given ensemble. We time-translate and average equivalent measurements on a given configuration into a single effective measurement prior to any further analysis. This helps to reduce the variance of the measured correlation functions. The only exception is that we use all available measurements to estimate the correlation matrix, as outlined in Appendix B.

C. Combined fits to two-point and three-point functions

For each of the operators Q_i^+, we extract the desired masses and matrix elements from a combined fit to several two-point and three-point functions. In particular, we jointly fit C_{PP}^{SL} C_{PP}^{SS} and C_{PA}^{SL} (C_{PP}^{LL} and C_{PA}^{LL} on F1M) and $C_3^i(t; \Delta T)$ for multiple choices of ΔT, typically parametrizing the ground state and the first excited state.[2] From these fits we extract the main quantities of interest: the bare bag parameters $\mathcal{B}_i^{\text{bare}}$; and the ratios of

---

[2]Since we only consider cases where either both propagators are smeared (local) at the operator "SS" ("LL") we simplify the notation and only use a single label per operator in the following.

operators R_i^{bare}. They are determined and quoted in the NPR basis (see Tables III and IV) but can subsequently be translated into the SUSY basis. For completeness we also quote the meson masses and bare decay constants at our simulation points for the pion and the kaon in Table XII in Appendix B.

We pursue two independent fit strategies and systematically vary the fit ranges of the two-point and three-point functions (including the choice of which source-sink separations enter the fit) until we see stability in all fit parameters. Figure 2 demonstrates this stability for the example of Q_2^+ on the C0M ensemble for the first strategy. The superimposed dashed lines and magenta bands in the first two panels correspond to the chosen fit if only the two-point functions are fitted. The green bands illustrate our preferred choice of fit. Each set of three data points corresponds to variations in the fit range for the three-point functions of $-1, 0, +1$ compared to the chosen fit. Finally, the different blocks correspond to our chosen fit; the same fit but only to the middle (first, last) half of the source-sink separations; additionally including an excited-to-excited matrix element; the same fit but for a varied choice of $t_{\min}$ for the two point functions which enter the fit. We find that the ground state fit results are insensitive to any of these choices. Further details are provided in Appendix B.

D. Valence strange quark correction

As is evident from Table II, the valence strange quark mass on the F1M ensembles is slightly mistuned from the physical strange quark mass value. We account for this effect by repeating the simulation at the physical strange quark mass on an eighth of the full statistics. We then compute the appropriate correction factors as

$$\alpha_{R_i} \equiv \frac{R_i^{\text{phys}}}{R_i^{\text{uni}}} = \lim_{0 \ll t \ll \Delta T} \frac{R_i^{\text{eff}}(t, \Delta T)|_{m_s^{\text{phys}}}}{R_i^{\text{eff}}(t, \Delta T)|_{m_s^{\text{uni}}}},$$

$$\alpha_{\mathcal{B}_i} \equiv \frac{\mathcal{B}_i^{\text{phys}}}{\mathcal{B}_i^{\text{uni}}} = \lim_{0 \ll t \ll \Delta T} \frac{\mathcal{B}_i^{\text{eff}}(t, \Delta T)|_{m_s^{\text{phys}}}}{\mathcal{B}_i^{\text{eff}}(t, \Delta T)|_{m_s^{\text{uni}}}}, \quad (3.6)$$
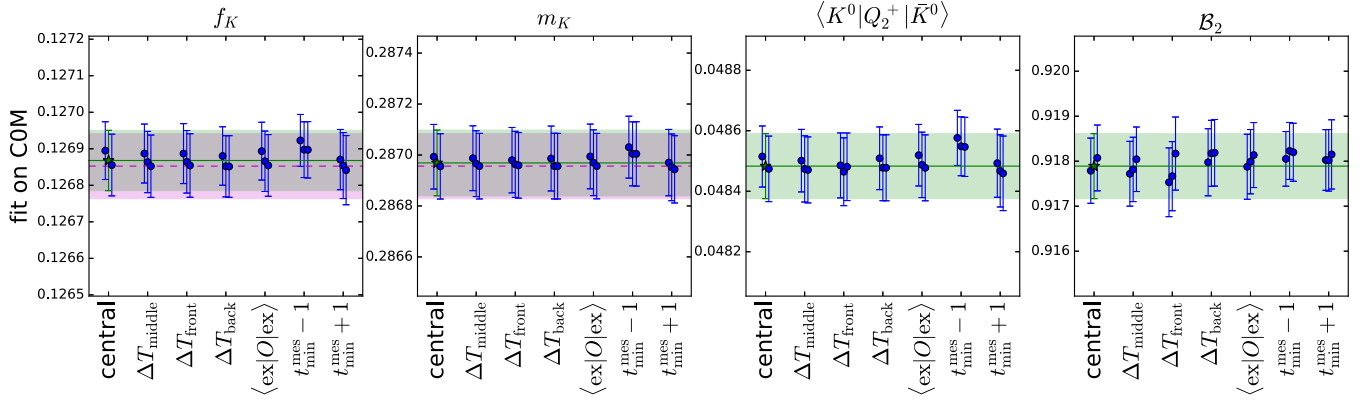
FIG. 2.   Stability of correlation function fits, illustrated on the example of the C0M ensemble for Q_2^+. All numbers are quoted in lattice units and the NPR basis.

where

$$R_i^{\text{eff}}(t, \Delta T) = \frac{C_3^i(t, \Delta T)}{C_3^1(t, \Delta T)},$$

$$\mathcal{B}_i^{\text{eff}}(t, \Delta T) = \frac{C_3^i(t, \Delta T)}{N_i C_2(t) C_2(\Delta T - t)}. \quad (3.7)$$

We find that the effect of the ∼3% mistuning of the strange quark valence mass leads to a ∼0.3–0.5% correction for the bag parameters and a ∼3% correction for the ratio of operators—see Table V. Given that the relative uncertainty of the correction factor is more than an order of magnitude smaller than that of the values it is applied to, we treat this correction factor as uncorrelated. Figure 3 illustrates this correction factor for the case of $\mathcal{B}_5$ and R_5.

IV. NONPERTURBATIVE RENORMALIZATION

In order to obtain a well-defined value in the continuum limit, it is necessary to renormalize the matrix elements $\langle \bar{K}^0 | Q_i^+ | K^0 \rangle$. While it is possible to use the Schrödinger functional to renormalize these operators nonperturbatively (see for example Ref. [56]), in this work we determine the matrix of renormalization factors Z_{ij} using the Rome-Southampton method [57] with nonexceptional kinematics (RI-SMOM) [58]. At some renormalization scale μ the renormalized matrix element is then given by

$$\langle \bar{K}^0 | Q_i^+ | K^0 \rangle^{\text{RI}}(\mu, a) = Z_{ij}^{\text{RI}}(\mu, a) \langle \bar{K}^0 | Q_j^+ | K^0 \rangle^{\text{bare}}(a). \quad (4.1)$$

Provided chiral symmetry breaking effects are negligible the matrix $Z_{ij}^{\text{RI}}(\mu, a)$ has a block diagonal structure—which is the case for the set-up at hand [33]. The scale μ should fall within the "Rome-Southampton window"

$$\Lambda_{\text{QCD}}^2 \ll \mu^2 \ll \left(\frac{\pi}{a}\right)^2, \quad (4.2)$$

in which the upper limit is relevant to control discretization effects and the lower limit ensures accurate perturbative matching to $\overline{\text{MS}}$.

For the technical definitions, numerical values of the renormalization constants and details of the extrapolation of the renormalization constants to the massless limit, we refer the interested reader to Secs. C 1–C 3 in Appendix C. There we also discuss two choices, called γ_μ and $\slashed{q}$, of the renormalization conditions imposed to precisely define the renormalization scheme.

A. Analysis of nonperturbative renormalization data

In practice, our data covers many values in the range 2 GeV ≲ μ ≲ 3 GeV (see Fig. 19 in Appendix C 2 for details). On the computationally most expensive ensembles C0M and M0M we simulate at $am_s^{\text{sea}}/2$ in the valence sector. On all other ensembles we have additional simulation points at am_l^{sea} and $2am_l^{\text{sea}}$. We use this data ensemble-by-ensemble to extrapolate the renormalization constants to the massless limit in which the renormalization constants are formally defined (see Fig. 4). The extrapolation of the data on the physical pion mass ensembles is

TABLE V.   Correction factors to be applied to the bare values of R_i and $\mathcal{B}_i$ on the F1M ensemble in the NPR basis in order to correct the observables to the physical strange quark mass.

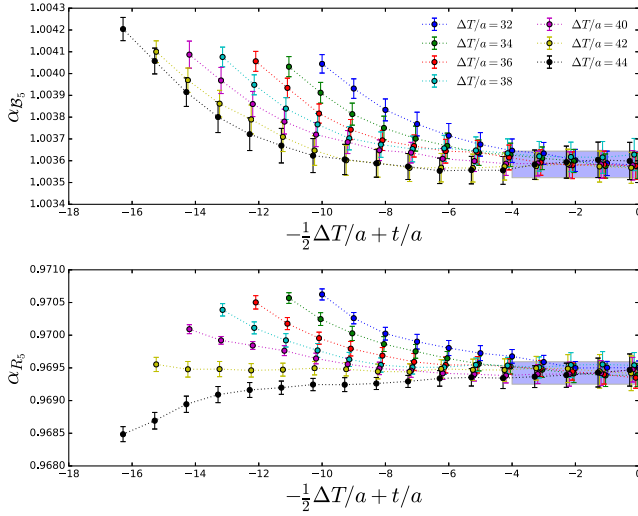| α_X	$i = 1$	$i = 2$	$i = 3$	$i = 4$	$i = 5$
$X = \mathcal{B}_i$	1.004983(99)	1.004231(66)	1.003036(65)	1.003193(71)	1.003583(61)
$X = R_i$		0.97005(18)	0.96890(18)	0.96904(17)	0.96942(17)

FIG. 3. Strange valence mistuning quark correction on the F1M ensemble for the example of $\mathcal{B}_5$ (top) and R_5 (bottom).
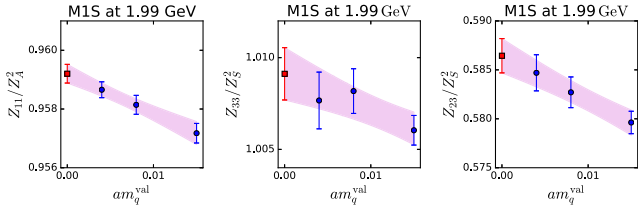

FIG. 4. Extrapolation of the renormalization constants to massless valence-quark limit for the example of the (11), (33) and (23) elements of the M1S ensemble close to 2 GeV. Results are presented in the RI-SMOM$^{(\gamma_\mu,\gamma_\mu)}$ scheme in the NPR basis.

performed by applying the slope of the C1M (M1M) ensemble to the C0M (M0M) data.

In a subsequent step we extrapolate the results for each action to zero sea light quark mass as is illustrated in Fig. 5 for the M-S ensembles at a momentum point close to 2 GeV. Since for the case of the F1M ensemble we only have a single sea quark mass data point, in practice we first interpolate the results on all ensembles to a common renormalization scale and then perform the sea-light quark mass to zero limit for each choice of distinct lattice spacing.
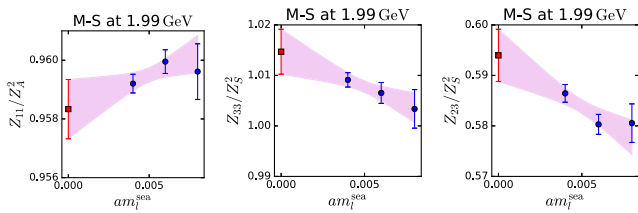

FIG. 5. Extrapolation of the renormalization constants to the zero light-sea quark mass limit for the example of the (11), (33) and (23) elements of the M-S ensembles close to 2 GeV. Results are presented in the RI-SMOM$^{(\gamma_\mu,\gamma_\mu)}$ scheme in the NPR basis.

For the F-M ensemble this is done by applying each of the four slopes (obtained from C-S, C-M, M-S and M-M) in turn and assigning a systematic uncertainty of half the spread of these results.

We list the chirally extrapolated renormalization constants for each lattice spacing at $\mu = 2$ GeV in Table VI (results for other values of μ can be found in Tables XVIII–XIX in Appendix C 3). Since these numbers contain information from multiple ensembles and the NPR calculations are based on a subset of the configurations, we propagate these small uncertainties in an uncorrelated fashion. To this end we add statistical and systematic uncertainties in quadrature and generate bootstrap samples for each of the Z_{ij} by drawing from a Gaussian distribution with the appropriate mean and width.

Finally, we use these values to renormalize the quantities of interest. In particular we find

$$R_i(\mu)^{\text{ren}} = \frac{Z_{ij}}{Z_{11}} R_j(\mu, a)|_{\text{bare}},$$

$$\mathcal{B}_1(\mu)^{\text{ren}} = \frac{Z_{11}}{Z_A^2} \mathcal{B}_1(\mu, a)|_{\text{bare}},$$

$$N_i \mathcal{B}_i(\mu)^{\text{ren}} = \frac{Z_{ij}}{Z_P^2} N_j \mathcal{B}_j(\mu, a)|_{\text{bare}} \quad i = 2, \dots, 5. \quad (4.3)$$

Here the N_i are the appropriate normalization factors defined above and in practice we make use of the relation $Z_S \approx Z_P$ due to chiral symmetry.

B. Step-scaling

When performing the renormalization we have the freedom to choose the renormalization scale μ within the Rome-Southampton window of our ensembles, which includes 2 GeV $\lesssim \mu \lesssim$ 3 GeV. We note that higher scales are more susceptible to discretization effects, while lower scales face larger errors when matching perturbatively to e.g. $\overline{\text{MS}}$.

We can scale the value of an operator renormalized at one scale to another with the use of a scale evolution matrix, $\sigma(\mu_2, \mu_1)$, in a procedure called step-scaling [59–61]. We define the continuum scale evolution matrix for the renormalization of the four-quark operators as

$$\sigma(\mu_2, \mu_1) = \lim_{a^2 \to 0} Z(\mu_2, a) Z^{-1}(\mu_1, a), \quad (4.4)$$

where $Z(\mu, a)$ is the 5×5 block-diagonal matrix described above. Therefore it is possible to scale our operators, once renormalized and extrapolated to the continuum limit, from μ_1 to μ_2. By renormalizing at $\mu = 2$ GeV, where lattice artefacts are less significant, but step-scaling our results in RI-SMOM to $\mu = 3$ GeV before perturbatively matching to $\overline{\text{MS}}$ we also avoid the higher errors associated with the truncation of the perturbative series at lower scales.

TABLE VI.   Elements of $Z_{ij}/Z^2_{A/S}$ extrapolated to the massless limit. All results are provided in RI-SMOM$^{(\gamma_\mu,\gamma_\mu)}$ at $\mu = 2.0$ GeV in the SUSY basis. The first parenthesis is the statistical error and the second is the systematic error. More detail is provided in Appendix C 3.

a^{-1} [GeV]	1.7295(38)	1.7848(50)	2.3586(70)	2.3833(86)	2.708(10)
Z_{11}/Z^2_A	0.93258(26)(0)	0.93444(77)(1)	0.96021(51)(2)	0.9579(12)(0)	0.97120(69)(47)
Z_{22}/Z^2_S	1.0703(26)(0)	1.0788(37)(2)	1.1185(18)(0)	1.1237(64)(1)	1.1405(27)(18)
Z_{23}/Z^2_S	−0.06092(49)(8)	−0.0603(10)(0)	−0.04045(55)(5)	−0.0387(10)(0)	−0.03054(62)(27)
Z_{32}/Z^2_S	0.0343(31)(3)	0.0403(74)(1)	0.1135(47)(1)	0.120(11)(0)	0.1522(57)(6)
Z_{33}/Z^2_S	1.6094(53)(13)	1.643(13)(0)	1.9107(85)(9)	1.948(21)(0)	2.064(10)(6)
Z_{44}/Z^2_S	1.0113(21)(2)	1.0161(35)(2)	1.0134(11)(0)	1.0160(51)(0)	1.0122(21)(16)
Z_{45}/Z^2_S	−0.07270(48)(4)	−0.07384(98)(6)	−0.06217(46)(7)	−0.06268(98)(0)	−0.05774(49)(44)
Z_{54}/Z^2_S	−0.23507(99)(38)	−0.2417(31)(1)	−0.2851(20)(2)	−0.2940(46)(2)	−0.3119(22)(15)
Z_{55}/Z^2_S	1.4762(38)(9)	1.4994(96)(6)	1.6718(64)(5)	1.699(15)(0)	1.7670(74)(55)

Since we have mapped out the region $2 \text{ GeV} \lesssim \mu \lesssim 3 \text{ GeV}$, we can further split (4.4) into multiple smaller steps $\Delta = (\mu_2 - \mu_1)/N$, i.e. we can compute the product

$$\prod_{k=0}^{N-1} \sigma(\mu_1 + k\Delta + \Delta, \mu_1 + k\Delta). \tag{4.5}$$

Alongside directly renormalizing at 3 GeV, we can also renormalize the result at 2 GeV and step scale to 3 GeV in one step, or in multiple steps as described above. This allows us to probe the effect the scale of the renormalization has. Details of the computation and numerical values for the step-scaling matrices are provided in Appendix C 4. The numerical values for the step-scaling matrices in the RI-SMOM$^{(\gamma_\mu,\gamma_\mu)}$-scheme and in the SUSY basis are given by

$$\sigma(3 \text{ GeV}, 2 \text{ GeV}) = \begin{bmatrix} 0.98021(53) & 0.0 & 0.0 & 0.0 & 0.0 \\ 0.0 & 0.9194(22) & -0.0630(16) & 0.0 & 0.0 \\ 0.0 & -0.00284(35) & 0.6846(19) & 0.0 & 0.0 \\ 0.0 & 0.0 & 0.0 & 0.9988(24) & 0.0784(25) \\ 0.0 & 0.0 & 0.0 & 0.00838(59) & 0.7542(24) \end{bmatrix}, \tag{4.6}$$

$$\sigma\left(3 \text{ GeV} \xleftarrow{\Delta=0.5 \text{ GeV}} 2 \text{ GeV}\right) = \begin{bmatrix} 0.98030(35) & 0.0 & 0.0 & 0.0 & 0.0 \\ 0.0 & 0.9199(22) & -0.0634(15) & 0.0 & 0.0 \\ 0.0 & -0.00260(31) & 0.6863(17) & 0.0 & 0.0 \\ 0.0 & 0.0 & 0.0 & 0.9990(25) & 0.0778(24) \\ 0.0 & 0.0 & 0.0 & 0.00860(44) & 0.7552(23) \end{bmatrix}. \tag{4.7}$$

V. CHIRAL CONTINUUM FITS AND FINAL RESULTS

A. Fit ansatz

To recover continuum results at physical quark masses we perform a simultaneous chiral-continuum limit fit. Our fit ansatz is based on NLO SU(2) chiral perturbation theory (χ_{PT}), covered in more detail in Ref. [29], and includes a chiral logarithm term. Furthermore our fit function is linear in a^2 and m_π^2 and the mistuning of the strange quark mass $\delta^{\text{sea}}_{m_s}$. It is given by

$$Y_i(a^2, m_\pi^2, m_s^{\text{sea}}) = Y_i^{\text{phys}}\left(1 + \alpha_i(a\Lambda)^2 + \beta_i \frac{m_\pi^2 - (m_\pi^{\text{phys}})^2}{(m_\pi^{\text{phys}})^2} + \gamma_i \delta^{\text{sea}}_{m_s} + L_i^Y(m_\pi) - L_i^Y(m_\pi^{\text{phys}})\right). \tag{5.1}$$

where $Y \in \{\mathcal{B}, R\}$ is the quantity of interest. Λ is a typical QCD-scale and we take the isospin-averaged pion mass to be $m_\pi^{\text{phys}} = (2m_\pi^\pm + m_\pi^0)/3 \approx 138$ MeV [62]. Y_i^{phys}, α, β and γ are fit parameters, $\delta_{m_s}^{\text{sea}} = (m_s^{\text{sea}} - m_s^{\text{phys}})/m_s^{\text{phys}}$ parameterizes the mistuning of the sea strange quark mass and the chiral logarithms are given by $L_i^Y(m_\pi) = C_i^Y m_\pi^2 \log(m_\pi^2/\Lambda^2)/(16\pi^2 f_\pi^2)$. The coefficients C_i are known constants with numerical values $C_i^{\mathcal{B}} = -0.5$ for $i = 1, 2, 3$ and $C_i^{\mathcal{B}} = 0.5$ for $i = 4, 5$ and we take $f_\pi = 130.41(23)$ MeV [62]. For the ratios R_2 and R_3 the chiral logarithms vanish ($C_2^R = C_3^R = 0$) and finally $C_4^R = C_5^R = 1$.

As stated in Sec. III the lattice spacings were determined in Ref. [7] (and updates thereof in Refs. [32,43]) from some of the same ensembles included in this work, hence a correlation between the data exists. However we perform an uncorrelated fit to decouple this work from the previous work. We propagate the error on the lattice spacing by generating bootstrap samples following a Gaussian distribution with width equal to the error on the lattice spacing. Given that the errors on the lattice spacings are of order 0.5% and all extrapolated quantities are dimensionless, we believe that neglecting these correlations has a negligible effect.

Our central fit results in the two intermediate schemes are obtained from a chiral-continuum limit fit at $\mu = 2$ GeV performed in the SUSY basis. These results are then step-scaled to 3 GeV [e.g. using the matrix provided in Eq. (4.6)] and perturbatively matched to $\overline{\text{MS}}$. In the following sections we will present the results of the chiral-continuum limit fits and assemble the full uncertainty budget relating to the lattice computation in the intermediate RI-SMOM schemes at 3 GeV. Only subsequently do we match these results perturbatively to $\overline{\text{MS}}$. This allows us to cleanly separate the uncertainties due to the perturbative matching to $\overline{\text{MS}}$ from those arising in the lattice calculation.

B. Results of the chiral-continuum limit fits

In this section we present the chiral-continuum limit fits in the RI-SMOM$^{(\gamma_\mu, \gamma_\mu)}$ scheme at $\mu = 2$ GeV and in the SUSY basis. We show these fits for the ratios R_i in Figs. 6 and 7 and for the bag parameters $\mathcal{B}_i$ in Figs. 8 and 9. Since we find that the C2S ensemble—which is at the heaviest pion mass and the coarsest lattice spacing—is not always well described by the fit ansatz, we remove it from our central fits. The data is well described by the fit function (5.1) in all cases with acceptable p-values ($> 5\%$) for all fits presented.
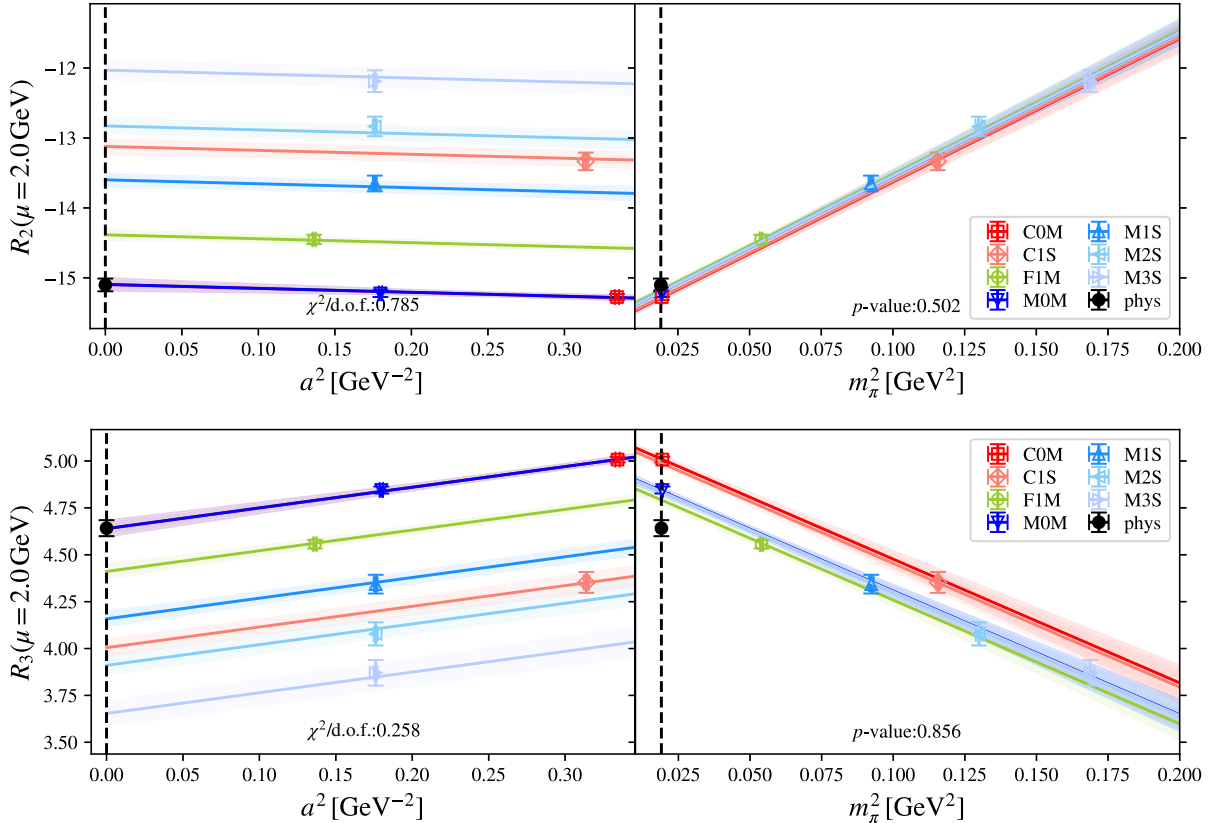

FIG. 6.   Chiral-continuum limit fit to BSM ratio parameters R_2 (top) and R_3 (bottom) in the SUSY basis, renormalized in the RI-SMOM$^{(\gamma_\mu, \gamma_\mu)}$ scheme.
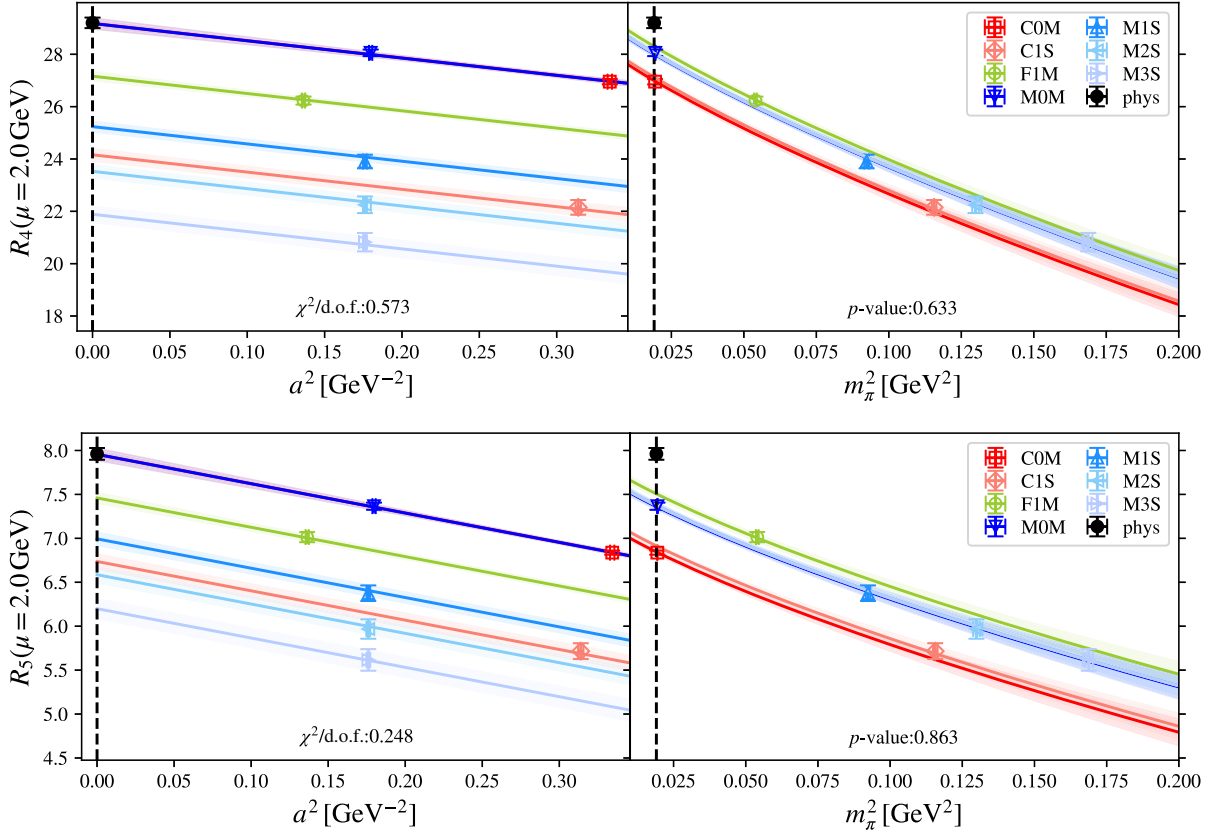
FIG. 7. Chiral-continuum limit fit to BSM ratio parameters R_4 (top) and R_5 (bottom) in the SUSY basis, renormalized in the RI-SMOM$^{(\gamma_\mu, \gamma_\mu)}$ scheme.

C. Error budget

In the following we quantify all relevant sources of uncertainties. We consider variations to the data and the fit ansatz; variations of the renormalization procedure; and uncertainties stemming from the perturbative matching. We quantify the uncertainties for the variations by considering

$$\delta_i^{\text{var}}(\mu) = \frac{|Y_i^{\text{central}} - Y_i^{\text{variation}}|}{\frac{1}{2}(Y_i^{\text{central}} + Y_i^{\text{variation}})}, \qquad (5.2)$$

where $Y \in \{\mathcal{B}, R\}$.

1. Chiral extrapolation

The two precise data points at physical pion masses make the mass extrapolation element of the fit very benign. We quantify the associated uncertainty by varying the pion mass cut to the data, removing terms from our fit form and by repeating the fits using the alternative correlator fit results (see Appendix B 3). For each of these variations we compute the associated δ [see Eq. (5.2)] which measures the shift in central value and list the corresponding values in Table VII. For all ratios and bag parameters this error is well below 1% and typically substatistical. For each observable we assign the maximum of those values as

the systematic uncertainty associated to the chiral extrapolation listed as "chiral" in Table IX.

2. Discretization effects

The good chiral symmetry of domain wall fermions constrains $O(a)$ and $O(a^3)$ terms to be small. The $O(a^2)$ effects are controlled and removed by our three lattice spacings present in the fit. Power counting suggests that $O(a^4)$ effects for hadronic physics scales with a 1.73 GeV coarsest inverse lattice spacing will remain small on all data points. However, the same is not necessarily true for hard, off-shell vertex functions where the momenta are chosen as the best compromise for a Rome-Southampton window. The leading unremoved discretization effects are thus likely to come from the nonperturbative renormalization, and may be probed by comparing different ways of renormalizing our data. Our central chiral-continuum limit fit is based on data renormalized at $\mu = 2$ GeV which is then step-scaled to 3 GeV by the step-scaling function $\sigma(3 \text{ GeV}, 2 \text{ GeV})$ presented in Eq. (4.6) for the bag parameters. We compare the results obtained this way to using the alternative prescription to obtain the scaling function [cf. Eq. (4.5)] with $N = 2, 3$ and to performing the continuum limit to data renormalized directly at $\mu = 3$ GeV. We compute and report the associated values for δ_i in Table VIII.
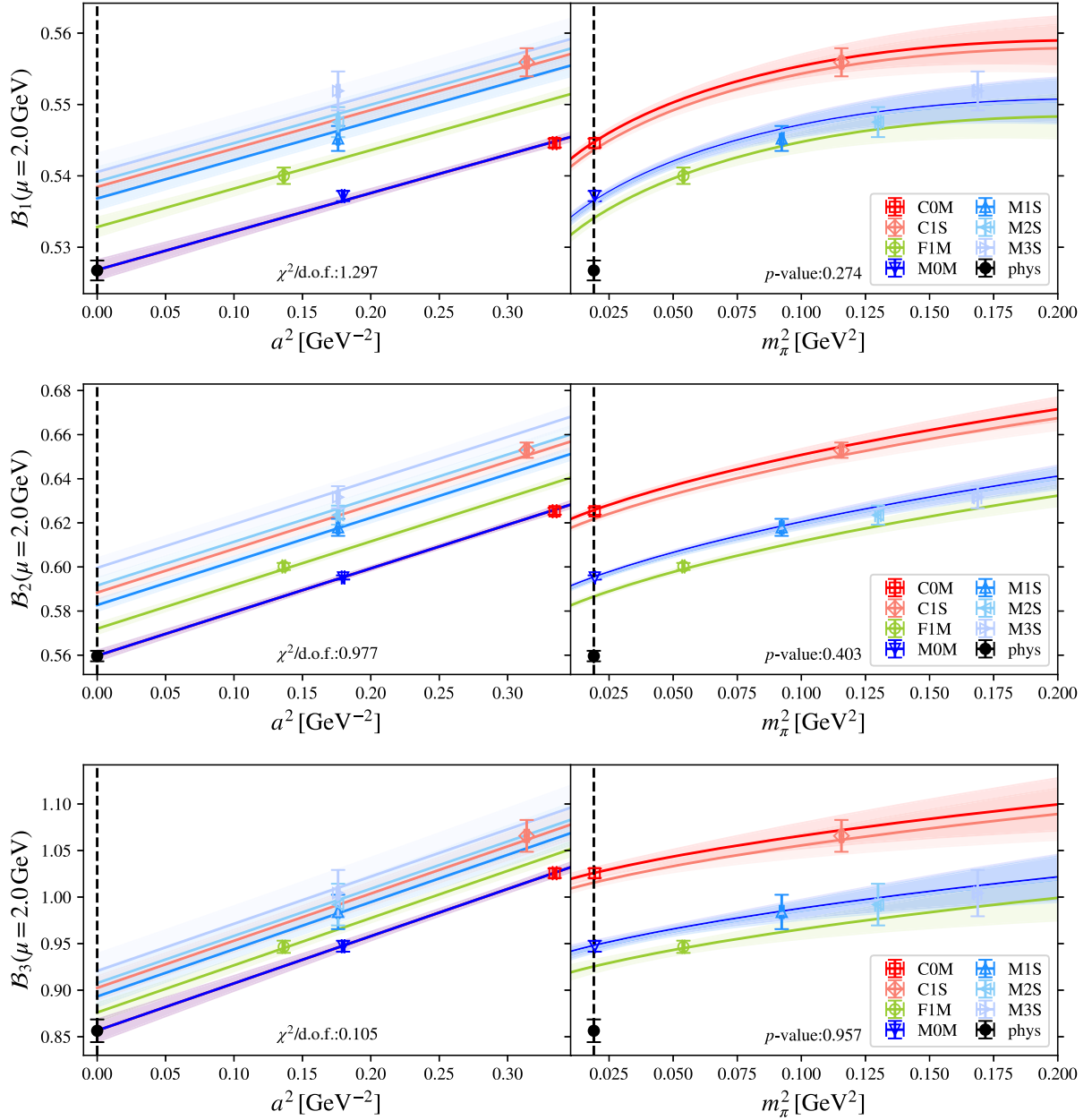
FIG. 8.   Chiral-continuum limit fit to the standard model bag parameter $\mathcal{B}_1$ (top) and BSM bag parameters $\mathcal{B}_2$ (middle) and $\mathcal{B}_3$ (bottom) in the SUSY basis, renormalized in the RI-SMOM$^{(\gamma_\mu,\gamma_\mu)}$ scheme.

For our main analysis we extract the bare matrix elements and renormalization factors in the NPR basis, transform them to the SUSY basis and then perform the various analysis steps. Performing the entire analysis in the NPR basis and converting the final values to the SUSY basis causes a reshuffling of discretization effects. The corresponding δ_i are presented in the column labeled SUSY ← NPR in Table VIII.

We take the maximum of these variations as estimate for the systematic uncertainties due to higher order discretization effects, labeled "discr" in Table IX.

3. Residual chiral symmetry breaking

Domain wall fermions provide a good approximation to chiral symmetry, however a small degree of residual chiral symmetry breaking is present in the data. Chiral symmetry restricts the allowed mixing pattern to be block-diagonal. For our central analysis we impose this, by setting the chirally forbidden elements of Z_{ij} to zero which we refer to as "masking." To test the effect residual chiral symmetry breaking has on our results, we repeat the entire analysis without masking. We find that the deviations are well below the percent level, indicating that our approximation to
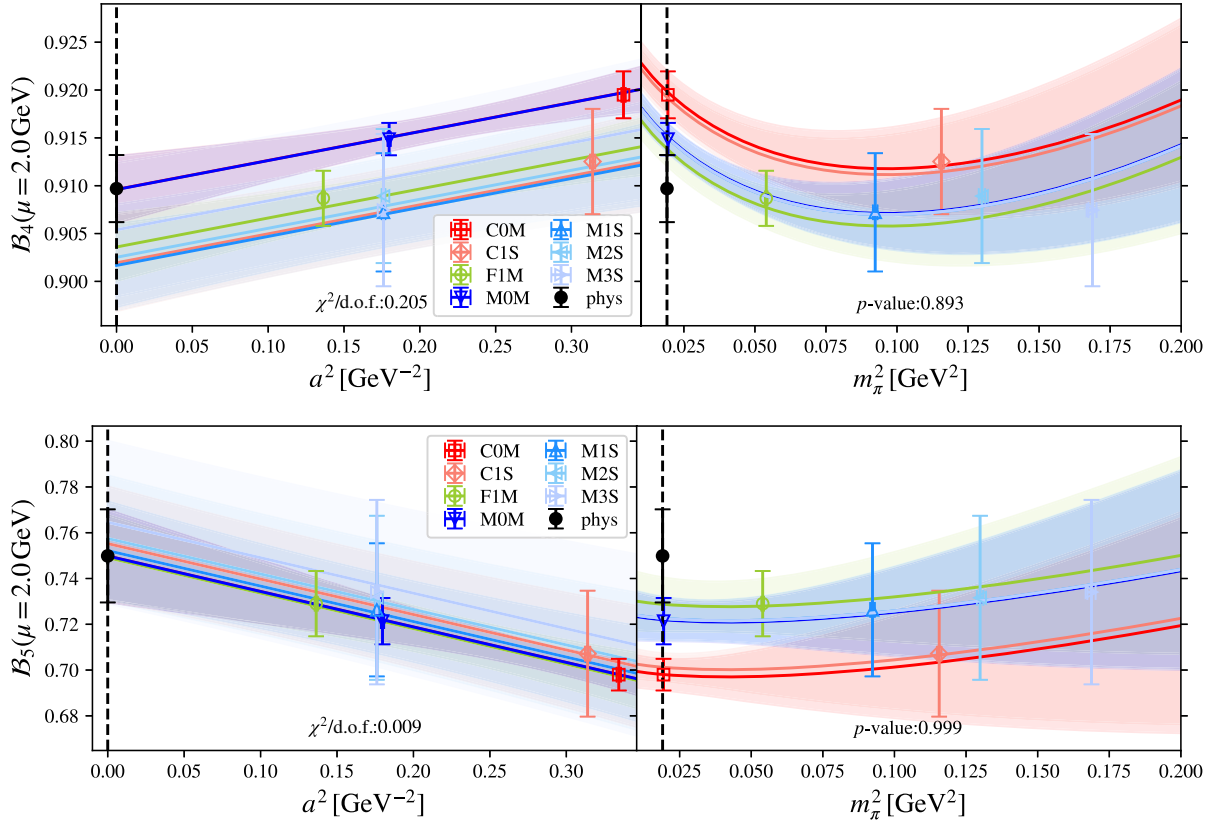
FIG. 9. Chiral-continuum limit fit to BSM bag parameters $\mathcal{B}_4$ and $\mathcal{B}_5$ in the SUSY basis, renormalized in the RI-SMOM$^{(\gamma_\mu \cdot \gamma_\mu)}$ scheme.

chiral symmetry is very well controlled. We report the associated systematic uncertainties in Tables VIII and IX as "rcsb."

4. Finite volume effects

Finite volume effects (FVEs) could be neglected in our previous studies, but at this level of precision we need to revisit this assumption. We estimate these effects using chiral perturbation theory and note that the finite volume corrections appear with the same prefactors C_i^Y as the chiral logarithms [40]. The FVEs are given by [63]

$$C_i^Y \frac{m_\pi^2}{(4\pi f_\pi)^2} \frac{12\sqrt{2\pi} \exp(-m_\pi L)}{(m_\pi L)^{3/2}}. \quad (5.3)$$

TABLE VII. Chiral-continuum limit fit systematics depending on choice of ansatz at $\mu = 2.0$ GeV in RI-SMOM$^{(\gamma_\mu \cdot \gamma_\mu)}$ in the SUSY basis. The first column shows the central value with statistical uncertainty, while the remaining columns quantify variations arising from different choices in the data that enters the fit as well as the model to which the chiral dependences is fitted. The last column illustrates the effect of using the alternative choice of correlation function fits underlying the analysis.

	Central fit	No δ_{m_s} (%)	No chiral logs (%)	$m_\pi < 440$ MeV (%)	$m_\pi < 370$ MeV (%)	$m_\pi < 350$ MeV (%)	Alternate fit (%)
R_2	$-15.106(87)$	0.22	$\cdots$	0.46	0.05	0.08	0.45
R_3	$4.643(41)$	0.42	$\cdots$	0.28	0.10	0.11	0.21
R_4	$29.22(19)$	0.51	0.59	0.58	0.04	0.06	0.49
R_5	$7.965(62)$	0.10	0.47	0.50	0.00	0.05	0.13
$\mathcal{B}_1$	$0.5268(13)$	0.10	0.21	0.49	0.02	0.06	0.40
$\mathcal{B}_2$	$0.5596(23)$	0.05	0.17	0.06	0.01	0.08	0.02
$\mathcal{B}_3$	$0.856(11)$	0.06	0.28	0.02	0.07	0.06	0.00
$\mathcal{B}_4$	$0.9097(35)$	0.03	0.17	0.08	0.01	0.02	0.06
$\mathcal{B}_5$	$0.750(19)$	0.02	0.24	0.18	0.02	0.03	0.13

TABLE VIII. Bag and ratio parameters at $\mu = 3$ GeV in RI-SMOM$^{(\gamma_\mu, \gamma_\mu)}$ in the SUSY basis. Central value comes from performing the chiral-continuum limit fit at $\mu = 2$ GeV and nonperturbative scaling the result to $\mu = 3$ GeV using $\sigma(3 \text{ GeV}, 2 \text{ GeV})$. We also list variations where the continuum step-scaling is obtained in steps, or the data is renormalized directly at 3 GeV. The central value uses Z-factors with chirally vanishing elements removed (masked) from $(P\Lambda)^T$ before the inversion $Z = F((P\Lambda)^T)^{-1}$. We list the percent shift in the result in foregoing this step, labeled residual chiral symmetry breaking (rcsb). We also compare with performing the entire analysis in the NPR basis and then rotating to the SUSY basis.

	$\sigma(3 \text{ GeV}, 2 \text{ GeV})$	$\sigma(3 \text{ GeV} \xleftarrow{\Delta=0.5} 2 \text{ GeV})$ (%)	$\sigma(3 \text{ GeV} \xleftarrow{\Delta=0.33} 2 \text{ GeV})$ (%)	NPR at 3 GeV (%)	rcsb (%)	SUSY $\leftarrow$ NPR (%)
R_2	$-18.37(10)$	0.12	0.13	0.17	0.11	0.02
R_3	$5.485(36)$	0.18	0.50	0.37	0.14	0.15
R_4	$38.60(27)$	0.02	0.02	0.48	0.09	0.01
R_5	$10.932(47)$	0.11	0.01	0.97	0.03	1.22
$\mathcal{B}_1$	$0.5164(14)$	0.00	0.01	0.01	0.04	0.01
$\mathcal{B}_2$	$0.5150(12)$	0.04	0.20	0.45	0.03	0.05
$\mathcal{B}_3$	$0.7624(52)$	0.32	0.24	1.51	0.06	0.15
$\mathcal{B}_4$	$0.9107(19)$	0.02	0.16	0.02	0.01	0.02
$\mathcal{B}_5$	$0.7792(79)$	0.11	0.24	0.38	0.00	0.26

TABLE IX. Central values and combined systematic errors for ratio and bag parameters in the SUSY basis at $\mu = 3$ GeV in the two RI-SMOM schemes—(γ_μ, γ_μ) and $(\not{q}, \not{q})$—as well as in $\overline{\text{MS}}$. For the RI-SMOM schemes we list the errors arising from statistics, chiral extrapolation, residual chiral symmetry breaking and discretization effects and combine them into total uncertainties. For the $\overline{\text{MS}}$ values we list the separate conversions from (γ_μ, γ_μ) and $(\not{q}, \not{q})$. The central values are defined as the average of those two numbers and the perturbative truncation error as half their difference. The lattice error is taken from the (γ_μ, γ_μ) scheme (see Table XXI for scheme-wise error budget).

Scheme		R_2	R_3	R_4	R_5	$\mathcal{B}_1$	$\mathcal{B}_2$	$\mathcal{B}_3$	$\mathcal{B}_4$	$\mathcal{B}_5$
RI-SMOM$^{(\gamma_\mu, \gamma_\mu)}$	Central	-18.37	5.485	38.60	10.93	0.5164	0.5150	0.762	0.9107	0.7792
	Statistical	0.59%	0.66%	0.72%	0.44%	0.28%	0.24%	0.69%	0.22%	1.02%
	Chiral	0.22%	0.42%	0.59%	0.47%	0.21%	0.17%	0.28%	0.17%	0.24%
	rcsb	0.11%	0.14%	0.09%	0.03%	0.04%	0.03%	0.06%	0.01%	0.00%
	discr	0.17%	0.50%	0.48%	1.22%	0.01%	0.45%	1.51%	0.16%	0.38%
	Total	0.66%	0.94%	1.05%	1.38%	0.35%	0.54%	1.68%	0.31%	1.11%
RI-SMOM$^{(\not{q}, \not{q})}$	Central	-19.53	5.818	40.99	10.49	0.5342	0.5155	0.765	0.9137	0.7078
	Statistical	0.68%	0.90%	0.81%	0.83%	0.29%	0.42%	1.20%	0.36%	2.19%
	Chiral	0.47%	0.77%	1.21%	1.23%	0.24%	0.27%	0.43%	0.28%	0.53%
	rcsb	0.28%	0.20%	0.23%	0.13%	0.08%	0.19%	0.28%	0.03%	0.01%
	discr	0.35%	0.66%	0.20%	2.25%	0.11%	0.63%	1.88%	0.19%	0.10%
	Total	0.94%	1.37%	1.48%	2.69%	0.40%	0.83%	2.29%	0.49%	2.25%
$\overline{\text{MS}}$	(γ_μ, γ_μ)	-18.73	5.781	41.45	10.80	0.5185	0.4759	0.728	0.8862	0.6977
	$(\not{q}, \not{q})$	-19.07	6.059	42.43	10.49	0.5295	0.4829	0.764	0.9070	0.6788
	Central	-18.90	5.920	41.94	10.64	0.5240	0.4794	0.746	0.8966	0.6882
	Lattice	0.66%	0.96%	1.06%	1.40%	0.34%	0.52%	1.75%	0.32%	1.14%
	PT	0.91%	2.35%	1.17%	1.47%	1.05%	0.74%	2.40%	1.16%	1.38%
	Total	1.12%	2.54%	1.57%	2.03%	1.10%	0.90%	2.97%	1.20%	1.79%

The leading order FVEs cancel in the ratios R_2 and R_3. Numerically evaluating Eq. (5.3) for our ensembles, we find that the largest effect is observed on the M1S ensemble, where the estimate of finite size effects is 1.1 per-mille for the bag parameters and 2.1 per-mille for R_4 and R_5. Noting that this is a sub-leading effect (cf. Table IX) and that the FVEs on the ensembles which are most constraining for the fit (C0M, M0M, F1M) are more than a factor three smaller than this, we conclude that FVEs remain negligible at our current level of precision.

5. Perturbative matching

The dominant source of uncertainty arises in the conversion of our results to $\overline{\text{MS}}$ where the matching is done in perturbation theory to one-loop. The truncation of the perturbative series leads to an uncertainty. We have defined two intermediate RI-SMOM schemes, differentiated by their projectors and use these to estimate the size of this error. We expect results in $\overline{\text{MS}}$ to be independent of the intermediate renormalization scheme. We take our central value as the average between the results obtained from the two intermediate schemes and associate a truncation uncertainty of half their difference. For definiteness we assign the relative error from the (γ_μ, γ_μ) scheme to quantify the combined lattice uncertainty in our final results. The estimate of the perturbative truncation uncertainty is quoted as "PT" in the last column of Table IX.

D. Self-consistency check

Having determined the R_i and the $\mathcal{B}_i$ parameters we can perform a self-consistency check. Recalling the definitions in Eqs. (2.7), (2.9), and (2.10) we consider

$$\frac{N_i \mathcal{B}_i}{R_i} = \frac{8}{3} \frac{(m_s(\mu) + m_d(\mu))^2}{m_K^2} \mathcal{B}_1, \quad i = 2, \ldots, 5. \quad (5.4)$$

The right hand side is independent of i and hence the ratios from each operator should give compatible results. The black data points in Fig. 10 display this comparison for the results at $\mu = 3$ GeV in RI-SMOM$^{(\gamma_\mu, \gamma_\mu)}$ (top) and $\overline{\text{MS}}$ (bottom). The R_i and $\mathcal{B}_i$ have notably different—and sometimes steep—approaches to the continuum limit. The good agreement between the different results gives us confidence that uncertainties in general and discretization effects in particular have been well estimated.

We compare our $\overline{\text{MS}}$ results to the value obtained by evaluating the right-hand side using external inputs. We use
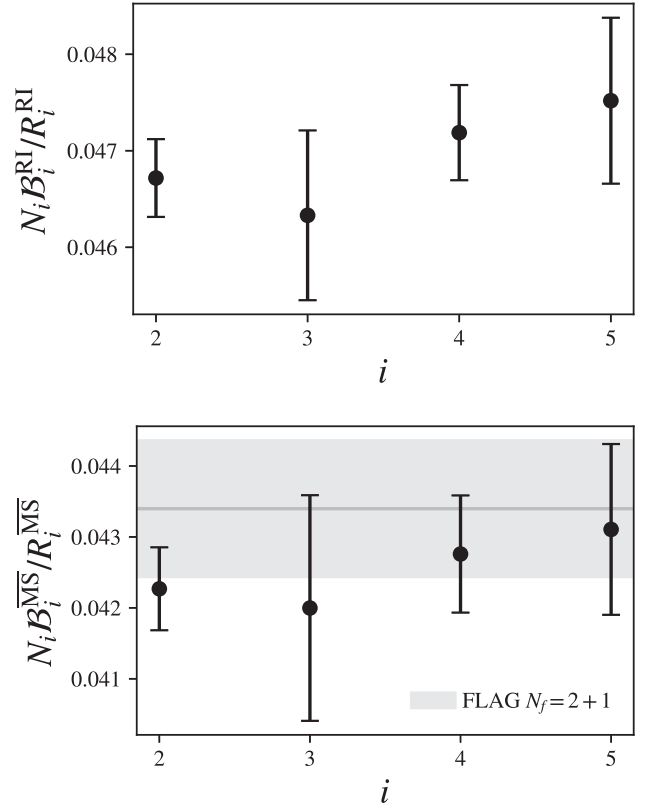

FIG. 10. Self-consistency check by forming the ratio Eq. (5.4) at $\mu = 3$ GeV. The data points are from our calculations in the RI-SMOM$^{(\gamma_\mu, \gamma_\mu)}$ scheme (top) and in the $\overline{\text{MS}}$ scheme (bottom). For the $\overline{\text{MS}}$ plot we show the expected value using FLAG inputs as the gray horizontal band.

the isospin-symmetrized kaon mass $m_K = (m_{K^0} + m_{K^\pm})/2 = 496.144(9)$ MeV [62]. We take FLAG [13] values for the $N_f = 2 + 1 + 1$ [11,64–69] and $N_f = 2 + 1$ [7,9,70–78] isospin-symmetrized light quark mass and strange quark mass in $\overline{\text{MS}}$ at $\mu = 2$ GeV, together with $\hat{B}_K$, the renormalization group invariant (RGI) value for $\mathcal{B}_1$,

$$N_f = 2 + 1 + 1: \quad m_{ud} = 3.410(43) \text{ MeV} \quad m_s = 93.44(68) \text{ MeV} \quad \hat{B}_K = 0.717(24),$$

$$N_f = 2 + 1: \quad m_{ud} = 3.364(41) \text{ MeV} \quad m_s = 92.03(88) \text{ MeV} \quad \hat{B}_K = 0.7625(97). \quad (5.5)$$

and run them to $\mu = 3$ GeV, allowing us to construct the right hand side of Eq. (5.4) [the conversion of the four-quark operators at a given scale to RGI operators is shown in Eq. (E21)]. This is shown as the gray band in the lower plot in Fig. 10.

Furthermore, we can use the constant value in both the RI-SMOM and $\overline{\text{MS}}$ schemes, combining it with our value for $\mathcal{B}_1$, to predict the sum of the quark masses (see also the discussion in Ref. [27]). From our result for $i = 2$ we find:

$$(m_s + m_{ud})^{\text{RI}}(3 \text{ GeV}) = 91.38(41) \text{ MeV},$$

$$(m_s + m_{ud})^{\overline{\text{MS}}}(3 \text{ GeV}) = 86.29(79) \text{ MeV}. \quad (5.6)$$

We compare this to the corresponding FLAG values

$$N_f = 2 + 1 + 1: (m_s + m_{ud})^{\overline{\text{MS}}}(3 \text{ GeV}) = 88.18(63) \text{ MeV},$$

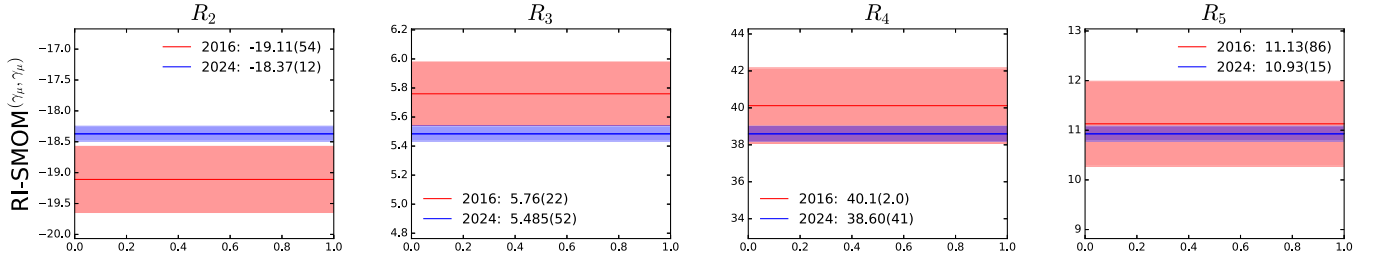$$N_f = 2 + 1: (m_s + m_{ud})^{\overline{\text{MS}}}(3 \text{ GeV}) = 86.34(79) \text{ MeV}. \quad (5.7)$$

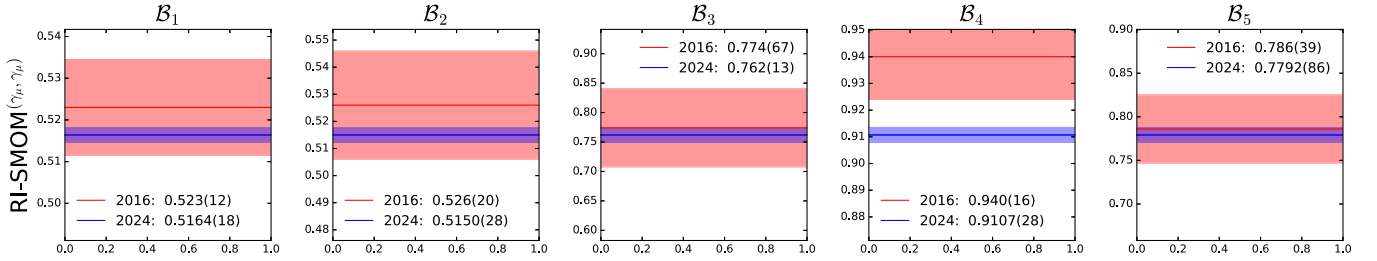FIG. 11.   Comparison of the R_i in RI-SMOM$^{(\gamma_\mu, \gamma_\mu)}$ at $\mu = 3$ GeV to our previous work [29].

FIG. 12.   Comparison of the $\mathcal{B}_i$ in RI-SMOM$^{(\gamma_\mu, \gamma_\mu)}$ at $\mu = 3$ GeV to our previous work [29].

E. Comparison to our previous work

In Figs. 11 and 12 we compare our results in the RI-SMOM scheme at $\mu = 3$ GeV to our previous determination [29]. The addition of two physical pion mass ensembles and a third lattice spacing helps to constrain the chiral and continuum limit extrapolations respectively, yielding a significantly reduced uncertainty. Given the significantly different dataset, we find good agreement between our previous result and this work.

F. Correlation between the different fit parameters

We provide the statistical correlation matrix between the $\mathcal{B}_i$, R_i and $\langle K | O_i^+ | \bar{K} \rangle$ as an ancillary hdf5 file and show the resulting correlation matrix in Fig. 13. For completeness we include results for RI-SMOM$^{(\gamma_\mu, \gamma_\mu)}$(2 GeV),
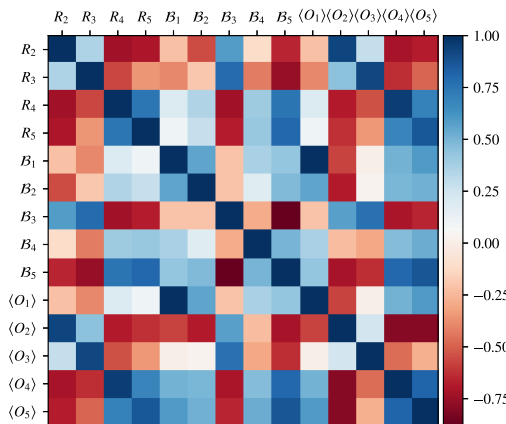

FIG. 13.   Heat-map of the statistical correlation matrix between the $\mathcal{B}_i$, R_i and the $\langle K | O_i^+ | \bar{K} \rangle$ in $\overline{\text{MS}}$ at 3 GeV.

RI-SMOM$^{(\gamma_\mu, \gamma_\mu)}$(3 GeV), RI-SMOM$^{(\not{q}, \not{q})}$(2 GeV) and RI-SMOM$^{(\not{q}, \not{q})}$(3 GeV) as well as $\overline{\text{MS}} \leftarrow$ RI-SMOM$^{(\gamma_\mu, \gamma_\mu)}$(3 GeV) and $\overline{\text{MS}} \leftarrow$ RI-SMOM$^{(\not{q}, \not{q})}$(3 GeV).

VI. CONCLUSIONS

In this paper we have performed the first calculation of the nonstandard model neutral kaon mixing matrix elements with data directly simulated with physical quark masses. Using an increased level of volume averaging, with many $\mathbb{Z}_2$ wall sources on each configuration, we have been able obtain much reduced statistical errors compared to our previous publications, even with physical quark masses.

All sources of systematic uncertainties have been estimated. For each of the bag parameters and ratios of matrix elements a simultaneous fit has been performed to the mass and lattice spacing dependence. Direct simulation at physical quark masses leaves the mass dependence of this extrapolation a negligible systematic. With the inclusion of a third lattice spacing we can test the validity of a^2 scaling and find that in the range covered by our data it works well. We assess discretization uncertainties by considering different renormalization points and/or different ways of obtaining the nonperturbative scaling matrix. The self-consistency check of comparing ratios $N_i \mathcal{B}_i / R_i$ increases our confidence that the discretization effects have been well estimated, since those ratios approach the continuum limit in notably different ways.

The dominant systematic error comes from perturbative matching from the RI-SMOM scheme to $\overline{\text{MS}}$ at the 3 GeV renormalization point. This key error was assessed by comparing two different intermediate RI-SMOM schemes

after continuum extrapolation. If the matching were nonperturbative the intermediate scheme would be irrelevant, but with truncated, perturbative matching the results differ due to the truncation error. The differences are of the order 1%–3%.

Our final results in the $\overline{\text{MS}}$ scheme at 3 GeV, where the first error is the RI-SMOM error and the second is the uncertainty from the matching to $\overline{\text{MS}}$, are

$$\mathcal{B}_1^{\overline{\text{MS}}} = 0.5240(17)(54)$$
$$\mathcal{B}_2^{\overline{\text{MS}}} = 0.4794(25)(35)$$
$$\mathcal{B}_3^{\overline{\text{MS}}} = 0.746(13)(17)$$
$$\mathcal{B}_4^{\overline{\text{MS}}} = 0.897(02)(10)$$
$$\mathcal{B}_5^{\overline{\text{MS}}} = 0.6882(78)(94)$$
$$R_2^{\overline{\text{MS}}} = -18.90(12)(17)$$
$$R_3^{\overline{\text{MS}}} = 5.92(05)(13)$$
$$R_4^{\overline{\text{MS}}} = 41.94(44)(46)$$
$$R_5^{\overline{\text{MS}}} = 10.64(14)(15). \tag{6.1}$$

Figure 14 shows a comparison of our BSM bag parameters with previous lattice results.

Our value for the SM bag parameter $B_K = \mathcal{B}_1$ shows good consistency with our collaboration's most-recent previous result, $B_K^{\overline{\text{MS}} \leftarrow \text{SMOM}^{(\not{q}, \not{q})}}(3 \text{ GeV}) = 0.530(11)$ [7]. A different fitting procedure in which the physical point data was over-weighted was employed in Ref. [7] and, while it also included the coarse and medium ensembles

included in this work, it included a different third lattice spacing with a heavier pion mass. Further, it combined additional coarser ensembles with a different gauge action in a global fit, and reweighting factors to adjust the sea strange mass to the physical values. In this work we instead leave the sea-strange mass dependence as a fit parameter. Given the differences in the underlying correlator data and the various fitting procedures, the consistency of the results is reassuring.

We convert our result above for B_K at scale $\mu = 3$ GeV to the RGI value $\hat{B}_K = 0.7436(82)$ [the conversion factor is the 11 element of the matrix in Eq. (E21)]. A comparison of our $\hat{B}_K$ with previous lattice results is shown in Fig. 15, where good agreement is seen. Values for $\hat{B}_K$ and the BSM $\mathcal{B}_i$ estimated in a large-N_c (number of colors) expansion may be found in Refs. [79,80].

The prospects for further improvements of this calculation are as follows: We believe that the RI-SMOM scheme results are sufficiently precise that there is no purpose in further reduction in the error within the isospin symmetric pure QCD approximation. Instead, strong isospin breaking and QED must be addressed if greater accuracy is required. For our final results a significant source of error stems from the perturbative matching to $\overline{\text{MS}}$. This could be addressed by raising the matching scale at which we convert operators. The convergence is logarithmic in the energy scale and this will not lead to a rapid improvement in the calculation. It would be better to accompany this with a two-loop calculation of the scheme change factors presented in Ref. [33]. The quadratic suppression in α_s would be more beneficial than an increase in the renormalization scale toward the b-threshold.
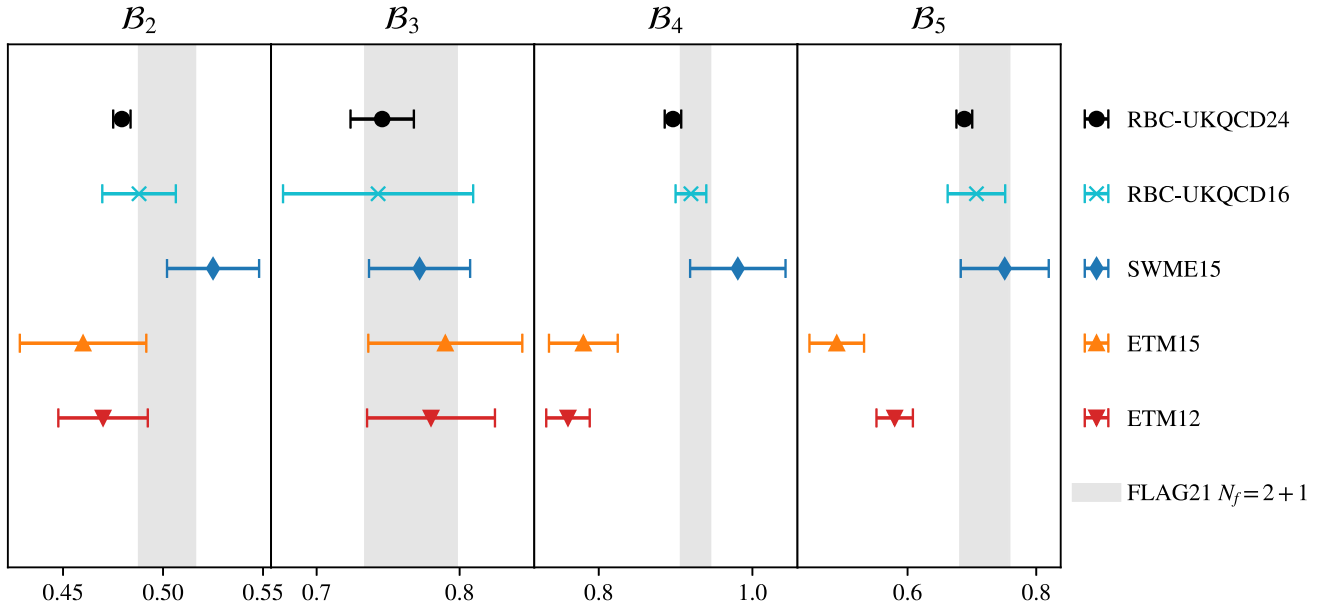

FIG. 14. Comparison of our results for the BSM bag parameters in $\overline{\text{MS}}$ at 3 GeV with previous results (RBC-UKQCD16 [29], SWME15 [9], ETM12 [12], ETM15 [11]).
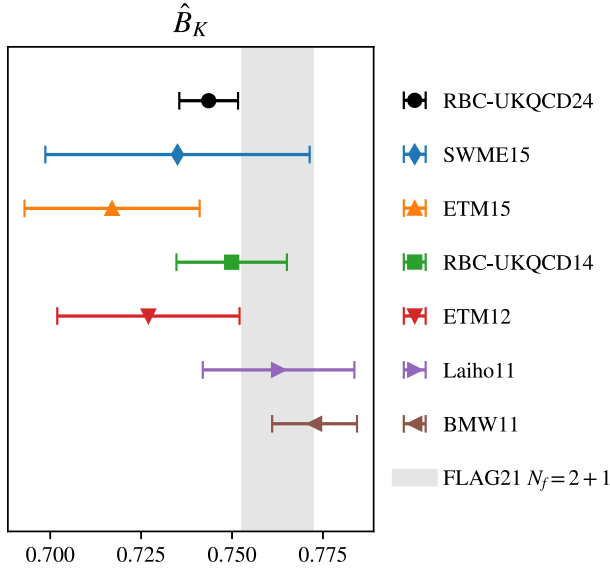
$\hat{B}_K$

FIG. 15. Comparison of our results for the RGI SM bag parameter $\hat{B}_K$ with previous results.

Consequently we believe our results are a robust determination that in the short term may only be further improved with an additional loop in the perturbative matching, or by the inclusion of isospin breaking effects.

This work is an important step toward the determination of the same observables in the $B^0_{(s)}$–$\bar{B}^0_{(s)}$ systems which is also being pursued by our collaboration [81,82].

ACKNOWLEDGMENTS

APPENDIX A: C1M AND M1M ENSEMBLES

RBC-UKQCD $2+1$f configurations initially used the standard domain wall fermion action with $L_s = 16$ [84], but when substantially lighter quark masses at physical values were introduced [7], it was desirable to reduce the level of residual chiral symmetry breaking and the Möbius domain wall fermion framework [48] was adopted with fixed independent Möbius parameter $b = 1.5$ and $c = 0.5$. We take $H_W = \gamma_5 D_W$ as the hermitian Wilson operator at negative domain wall mass, and with this choice of b and c this yields a kernel H_M entering the overlap sign function that is identical to the kernel H_T of standard domain wall fermions in the large L_s limit, with

$$H_M = \frac{2H_W}{2 + D_W} = 2H_T, \tag{A1}$$

entering the four dimensional effective overlap action via an approximate sign function which (if exact) removes the rescaling factor

$$D_{ov} = \frac{1 + m}{2} + \frac{1 - m}{2}\gamma_5\epsilon(H_M). \tag{A2}$$

Here the sign function approximation $\epsilon(H_M)$ is the tanh approximation to the exact sign function,

$$\begin{aligned}\epsilon(H_M) &= \frac{(1 + H_M)^{L_s} - (1 - H_M)^{L_s}}{(1 + H_M)^{L_s} + (1 - H_M)^{L_s}} \\ &= \tanh\left(L_s\tanh^{-1}H_M\right). \tag{A3}\end{aligned}$$

The four dimensional effective action of two actions coincide exactly when the extent of the fifth dimension is infinite, and at finite L_s differ only by terms that are exponentially suppressed in the fifth dimension extent, a scale which can by measured by the residual mass measured as the defect of the Möbius chiral Ward identity [7]. Indeed on these two new ensembles, we obtain residual masses which are very close to those of the corresponding physical pion mass ensembles [7] as can be seen from Table XI.

Previously RBC-UKQCD have directly combined calculations on ensembles with the Shamir formulation of domain wall fermions at heavier quark masses with physical quark mass ensembles using the about Möbius action. This cost saving measure is reasonable at the percent scale level accuracy sought at the time, with residual chiral symmetry breaking effects being of lower magnitude and around 3×10^{-3} in the worst-case coarsest ensemble. In these initial ensembles, since the input quark mass that corresponds to the physical strange quark mass is determined by simulation, the strange quark mass could

TABLE X. Simulation and HMC parameters for the C1M and M1M ensembles.

Ensemble	C1M	M1M
Volume	$24^3 \times 64$	$32^3 \times 64$
β	2.13	2.25
b	1.5	1.5
c	0.5	0.5
L_s	24	12
M_5	1.8	1.8
m_l	0.005	0.004
m_s	0.0362	0.02661
m_h	$\{0.02, 0.2, 0.6\}$	$\{0.02, 0.2, 0.6\}$
N_{Traj}	1990	1950
Fermion steps	12	10
Sexton-Weingarten ratio	8	8
Integrator	Force gradient	Force gradient

only be approximately tuned in advance of their generation and so differed from the physical value. However, longer term there is great simplicity in generating new ensembles so that comparisons can be made and extrapolations performed with fewer variables changing (volume, residual chiral symmetry breaking, strange quark masses), while increased computing power made this now relatively easily affordable.
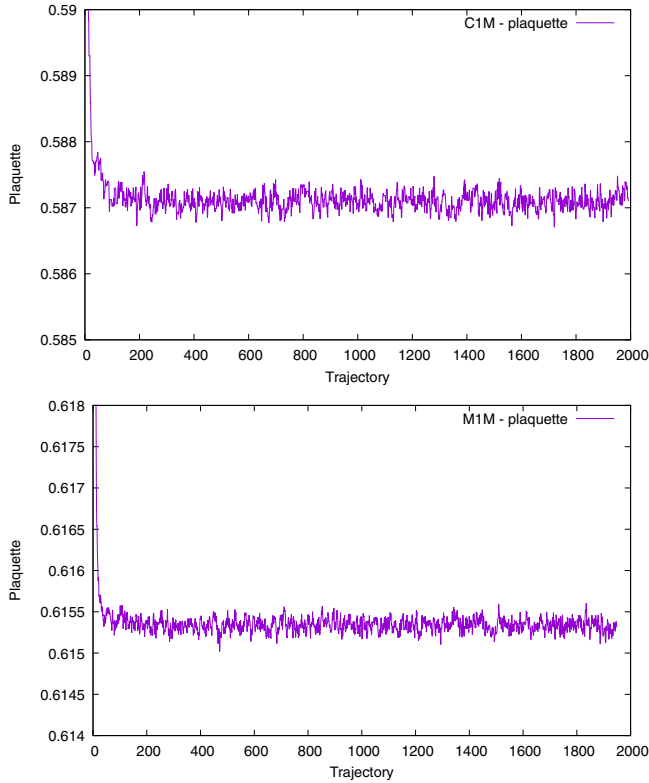

FIG. 16. Plaquette molecular dynamics time history for the C1M (top) and M1M (bottom) ensembles.

TABLE XI. Average plaquettes for the new M1M and C1M ensembles are more than adequately consistent with the (more precise) values obtained on the corresponding large volume and physical quark mass ensembles, given the volume and mass differ.

Ensemble	Plaquette	Residual mass
C0M	0.5871119(25)	0.0006102(40)
C1M	0.587091(7)	0.000604(11)
M0M	0.6153342(21)	0.0003116(23)
M1M	0.615337(4)	0.0003063(53)

To an extent chiral effective approaches and other methods can both estimate finite volume effects to be small and allow to correct for them. We therefore continue to use smaller volumes $24^3 \times 64$ for C1M and $32^3 \times 64$ for M1M, but took the opportunity to eliminate two of these three confounding effects that arise when using the older ensembles. The first is to keep the same residual chiral symmetry breaking approximation to the overlap operator, and the second is to retune the dynamical strange quark mass to its physical value on each ensemble, matching that used in the physical point ensembles C0M and M0M.

The new ensembles were generated using the GRID library [50], with simulation parameters and intermediate two flavor determinant Hasenbusch masses [85] that are given in Table X. The exact one flavor algorithm [86] was used for the strange quark using the implementation in GRID [87].

For M1M, a two level nested integrator was used in the HMC with the force gradient integrator [88,89], all pseudofermion action fragments taking ten steps with time step $\delta t = \frac{1}{10}$, and eight gauge steps for each fermion step. For C1M, a two level nested integrator was used in the HMC with the force gradient integrator, all pseudofermion action fragments taking twelve steps with time step $\delta t = \frac{1}{12}$, and eight gauge steps for each fermion step.

The first 200 trajectories were discarded from a hot start before measurements. The plaquette histories are shown in Fig. 16, and the average values are more than adequately consistent with those obtained more precisely in a larger volume at physical quark mass, Table XI, given that the quark mass and volume differ.

APPENDIX B: CORRELATION FUNCTION FITS

This section discusses the choices required in the correlation function fits. We commence by illustrating the quality of our data. In Sec. B 1 we discuss the construction of the covariance matrix used in these fits. To mitigate any bias stemming from fit range choices, two of the authors independently did the analysis of the correlation function fits. This resulted in two different fit strategies which will be outlined in Appendixes B 2 and B 3.

Figure 17 shows the bare effective ratios $R_i^{\mathrm{eff}}(t, \Delta T)$ [cf. Eq. (3.7)] in the NPR basis for the C0M (left) and M0M
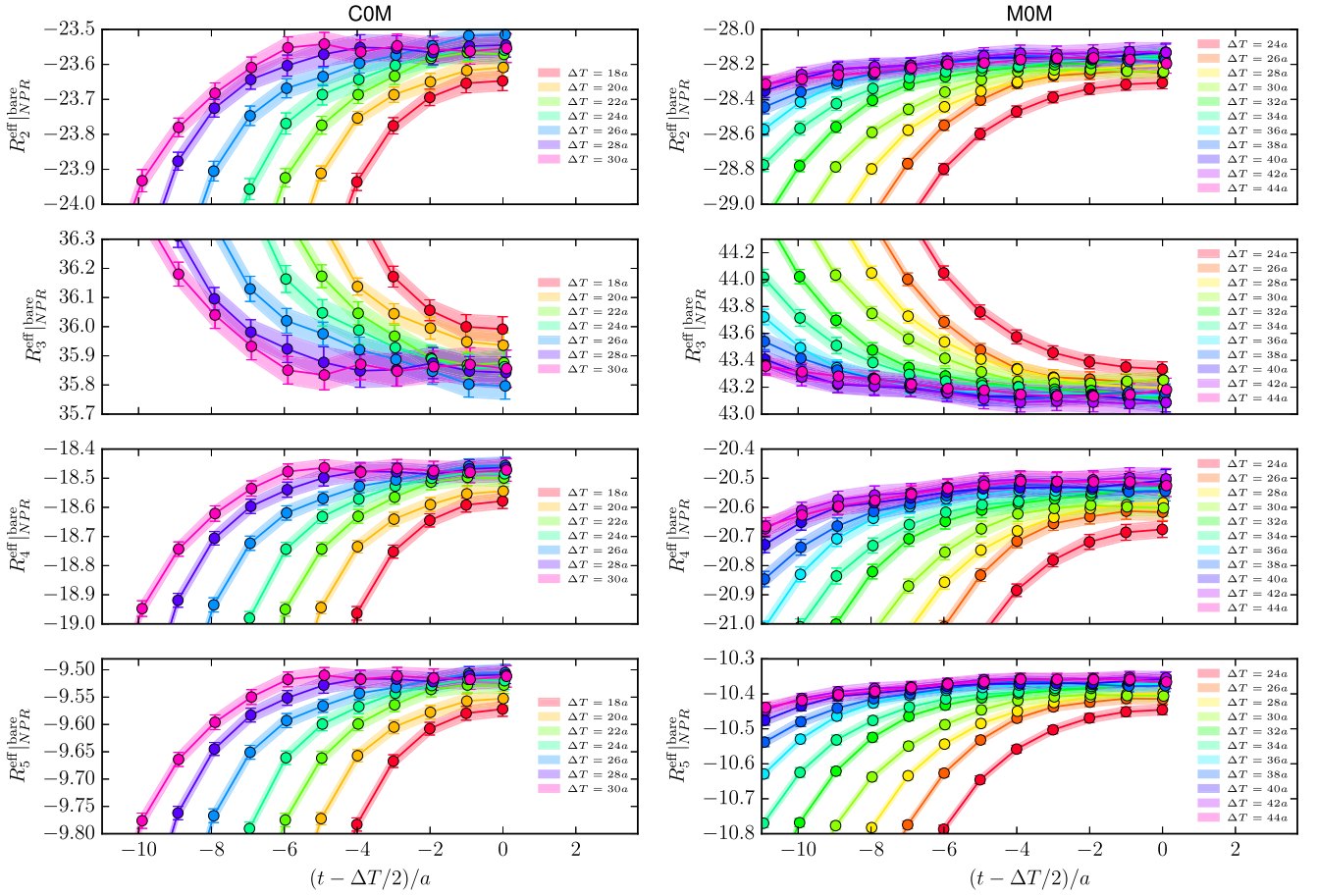
FIG. 17.   Illustration of the quality of our data for the C0M (left) and M0M (right) ensembles. We show the bare effective ratios $R_i^{\text{eff}}(t, \Delta T)$ in the NPR basis as defined in Eq. (3.7).

(right) ensembles for various typical source-sink separations ΔT. For sufficiently large ΔT values these ratios plateau to the same value, indicating ground-state saturation.

1. Correlated fits to data

In all of this paper, our fits are correlated frequentist minimizations of the χ^2-function

$$\chi^2 = \sum_{i,j}(f(a;x_i) - y_i)\text{cov}(y_i, y_j)^{-1}(f(a;x_j) - y_j), \quad \text{(B1)}$$

where y_i are our data, $f(a;x_i)$ is the model with parameters a that is being fitted and $\text{cov}(y_i, y_j)$ is the covariance matrix of the data. Resampling N statistical estimators into N_{boot} bootstrap samples $\tilde{y}_i$ and denoting the mean of y_i by $\bar{y}_i$, we define the covariance matrix $\text{cov}(y_i, y_j)$ as

$$\text{cov}(y_i, y_j) = \frac{1}{N_{\text{boot}}}\sum_{k=1}^{N_{\text{boot}}}((\tilde{y}_i)_k - \bar{y}_i)((\tilde{y}_j)_k - \bar{y}_j). \quad \text{(B2)}$$

We relate the covariance matrix to the standard deviation σ via $\sigma_i = \sqrt{\text{cov}(y_i, y_i)}$. Furthermore we define the *normalized covariance matrix* or *correlation matrix* $\text{cor}(y_i, y_j)$ as

$$\text{cor}(y_i, y_j) = \text{diag}(1/\sigma_i)\text{cov}(y_i, y_j)\text{diag}(1/\sigma_j). \quad \text{(B3)}$$

Since we jointly fit multiple two-point and three-point functions, it is important to be able to accurately invert the covariance matrix that appears in the χ^2-function.

On a given ensemble, we have $N_{\text{meas}} = N_{\text{conf}} \times N_{\text{src}}$ estimators for the y_i (compare Table II). When estimating the correlation matrix and the standard deviations, we therefore need to choose whether we treat measurements on different time translations on the same configuration as independent or whether we bin them into an effective measurement. From these two choices we obtain $(\sigma_i, \text{cor}(y_i, y_j))^{\text{unbinned}}$ and $(\sigma_i, \text{cor}(y_i, y_j))^{\text{binned}}$ based on $N_{\text{conf}} \times N_{\text{src}}$ measurements and N_{conf} effective measurements, respectively. Our reasoning is based on stochastic locality [90], i.e. the fact that observables measured in sufficiently distant regions of a gauge field configuration
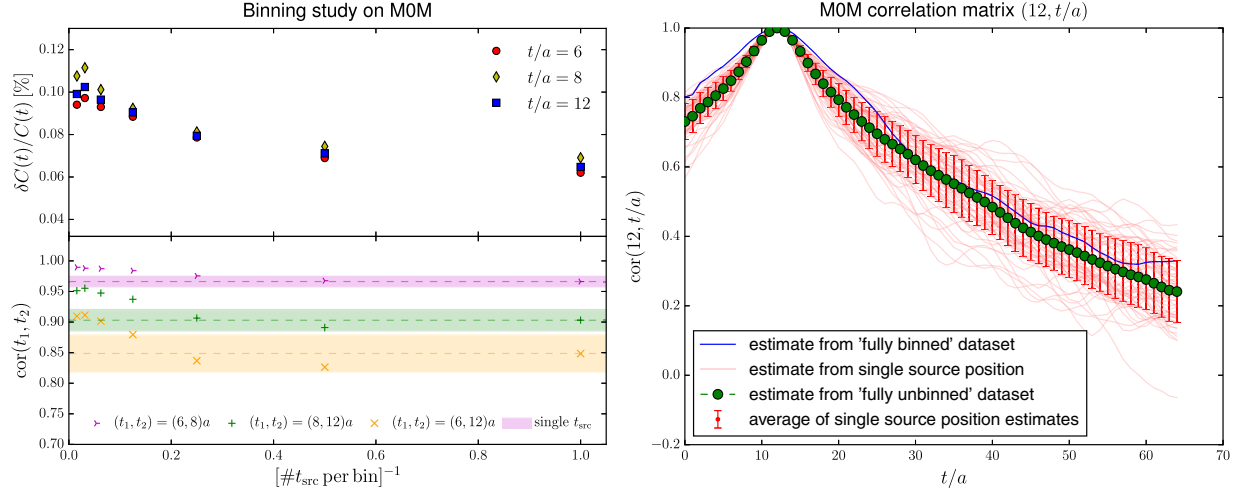
FIG. 18.   Investigation of binning choices for a typical Kaon two-point function on the M0M ensemble. Further details are provided in the text.

can be treated as independent. The separation that is required for this statement to hold, strongly depends on the observable under consideration. Since we only have access to measurements with sources shifted in the time direction, we are not pursuing a master field analysis [91] but instead use binning studies to gain insight into the level of independence of different measurements on the same configuration. When considering the covariance matrix that enters the χ^2 function, we consider two parts: the overall normalization, stemming from the estimate of the variances, and the normalized *correlation* matrix that measures the degree of correlations between different time slices. This separation is motivated by the following observation. If each measurement of a dataset with N_{conf} independent measurements is duplicated and (falsely) assumed to constitute a dataset with $2N_{conf}$ independent measurements then the mean values and the correlation matrix will remain unchanged, while the variance of the mean will be underestimated by a factor 2. The variance is hence far more sensitive to the assumption of statistical independence which causes us to assess the properties of the covariance of the mean and the correlation matrix separately.

The left-hand plot of Fig. 18 shows a binning study on the M0M ensemble. In the top panel the relative uncertainty of the pseudoscalar-pseudoscalar kaon two-point function is shown as a function of the inverse bin-size. The right-most data points correspond to considering every measurement as independent, whereas the left-most data point corresponds to the "fully binned" case, i.e. where all measurements on a given configuration are averaged into a single effective measurement. We find that the uncertainty only mildly depends on the bin size, but take the conservative approach of taking the variance from the maximally binned version of the dataset, in order to ensure that the uncertainties are not underestimated.

We now turn our attention to the correlation matrix. The right hand plot of Fig. 18 shows a slice of the correlation matrix where one time index is fixed to be $t/a = 12$. The blue solid line shows the estimate of the correlation matrix based on the "fully binned" case. The green dashed line with the circles on it, shows the "fully unbinned" estimate of the correlation matrix. The faint red lines correspond to estimates based on a single source plane, i.e. only include one measurement per configuration and are therefore based on a substatistic of $1/N_{src}$ measurements. Comparing these N_{src} estimators of the correlation matrix, allows us to obtain an indication of the uncertainty of the correlation matrix elements which is indicated by the red error bars. We note that the "fully unbinned" estimate agrees very well with this average.

In the bottom panel of the left-hand plot we perform the binning study for three representative elements of the correlation matrix and superimpose the uncertainty obtained from the N_{src} estimates as horizontal bands. In each case, we find that for sufficiently small number of sources per bin the values stabilize. We therefore conclude to use "fully unbinned" estimates for the correlation matrix, while using the "fully binned" estimate of the variance. We now construct the covariance matrix we use in the fit to the correlation functions as

$$\mathrm{cov}(y_i, y_j) = \mathrm{diag}(\sigma_i^{\mathrm{binned}})\mathrm{cor}(y_i, y_j)^{\mathrm{unbinned}}\mathrm{diag}(\sigma_j^{\mathrm{binned}}).$$

$$(B4)$$

This has the benefit that it resolves the correlations but estimates the statistical uncertainties without any assumption of independence for measurements from different source positions on the same configurations.

2. Correlation function fits—Strategy and stability

We jointly fit several two-point and three-point functions directly to their functional forms given by Eqs. (3.3) and (3.5). In a first step, we start by only fitting the two-point functions. We determine fit ranges $t_{\min}^{2\text{pt}}$ and $t_{\max}^{2\text{pt}}$ for the two-point functions which produce stable ground and first excited state results for masses and overlap factors. For each four-quark operator Q_i^+ we then perform a joint fit to the same two-point functions but also the corresponding three-point functions $C_3^i(t, \Delta T)$ for several values of ΔT. As a first step, we keep $t_{\min}^{2\text{pt}}$, $t_{\max}^{2\text{pt}}$ from above for the two-point functions. For the three-point functions we use the same $t_{\min}^{3\text{pt}}$ irrespective of ΔT. This is determined by choosing an integer δ to set $t_{\min}^{3\text{pt}} = t_{\min}^{2\text{pt}} + \delta$ and $t_{\max}^{3\text{pt}} = \Delta T - t_{\min}^{3\text{pt}}$. Typically we have $\delta \in \{0, 1\}$. We then vary δ by ± 1, vary the choice of which values of ΔT enter the fit and vary $t_{\min}^{2\text{pt}}$ by ± 1. We adjust these choices until we see stability in all fit parameters.

For completeness we summarize the meson masses $m_P = E_0$ and the bare decay constants f_P^{bare} for the pion and the kaon in Table XII.

3. Alternative strategy

We define the ratios of two-point functions (3.3) and three-point functions (3.5)

$$r^1(t, \Delta T) = \frac{C_3^1(t, \Delta T)}{C_{PA}(t)C_{AP}(\Delta T - t)},$$

$$r^i(t, \Delta T) = \frac{C_3^i(t, \Delta T)}{C_{PP}(t)C_{PP}(\Delta T - t)}, \qquad i > 1 \qquad \text{(B5)}$$

TABLE XII. Masses and bare decay constants of the pion and kaons for all of the ensembles used in this work.

Ensembles	am_π	af_π^{bare}	am_K	af_K^{bare}
C0M	0.08048(10)	0.10654(12)	0.28696(13)	0.126852(89)
C1S	0.19052(40)	0.11902(27)	0.30630(39)	0.13201(22)
C2S	0.24159(38)	0.12743(20)	0.32518(35)	0.13737(18)
M0M	0.059078(74)	0.074620(86)	0.21065(10)	0.089081(60)
M1S	0.12750(35)	0.08292(28)	0.22491(36)	0.09379(20)
M2S	0.15123(36)	0.08680(22)	0.23208(35)	0.09578(17)
M3S	0.17238(42)	0.09023(25)	0.23994(40)	0.09775(20)
F1M	0.08581(16)	0.06768(15)	0.18810(19)	0.07821(15)
C1M[a]	0.15987(50)	0.11659(60)	0.30560(51)	0.13261(52)
M1M[a]	0.12116(52)	0.07943(39)	0.22778(62)	0.09193(32)

[a]These ensembles only enter the analysis in order to constrain the chiral extrapolation of the renormalization constants described in Sec. IV.

which are constructed to asymptotically approach the bag parameters

$$r^i(t, \Delta T) \xrightarrow[0 \ll t \ll \Delta T \ll T]{} N_i \mathcal{B}_i. \qquad \text{(B6)}$$

For simplicity we omit the smearing labels s_1, s_2, which are chosen to ensure that only local matrix elements remain. Expanding numerator and denominator of the first line of Eq. (B5) using Eqs. (3.3) and (3.5) taking into account the ground state $(|0\rangle)$ and first excited state $(|1\rangle)$ contributions $(n = 0, 1)$ (but neglecting the excited-to-excited matrix elements) yields

$$r^1(t, \Delta T) = \frac{\langle 0|\mathcal{O}_1|0\rangle}{M_{A,0}^2} [1 + X_1(t, \Delta T)e^{-\Delta E \Delta T/2} + Y_1(t, \Delta T)e^{-\Delta E \Delta T}], \qquad \text{(B7)}$$

where we defined

$$X_1(t, \Delta T) = 2\frac{M_{P,1}E_0}{M_{P,0}E_1}\cosh[\Delta E(t - \Delta T/2)]\left(\frac{\langle 0|\mathcal{O}_1|1\rangle}{\langle 0|\mathcal{O}_1|0\rangle} - \frac{M_{A,1}}{M_{A,0}}\right),$$

$$Y_1(t, \Delta T) = -4\frac{M_{P,1}^2 E_0^2}{M_{P,0}^2 E_1^2}\cosh^2[\Delta E(t - \Delta T/2)]\frac{\langle 0|\mathcal{O}_1|1\rangle}{\langle 0|\mathcal{O}_1|0\rangle}\frac{M_{A,1}}{M_{A,0}}, \qquad \text{(B8)}$$

and $\Delta E = E_1 - E_0$. The expression for r^i $(i > 1)$ is very similar. Defining a summed version of the ratio

$$r^i(t_c, \Delta T) \equiv \sum_{t=t_c}^{\Delta T - t_c} r^i(t, \Delta T) \qquad \text{(B9)}$$

and using the identity

$$\sum_{t=t_c}^{\Delta T - t_c} \cosh[\Delta E(t - \Delta T/2)] = \frac{\sinh[\Delta E/2(\Delta T - 2t_c + 1)]}{\sinh[\Delta E/2]} \qquad \text{(B10)}$$

the summed ratio can be expressed as

$$r^1(t_c, \Delta T) = \frac{\langle 0|\mathcal{O}_1|0\rangle}{M_{A,0}^2}\left[\hat{t} + 2\frac{M_{P,1}E_0}{M_{P,0}E_1}e^{-\Delta E\Delta T/2}\frac{\sinh[\Delta E/2\hat{t}]}{\sinh[\Delta E/2]}\left(\frac{\langle 0|\mathcal{O}_1|1\rangle}{\langle 0|\mathcal{O}_1|0\rangle} - \frac{M_{A,1}}{M_{A,0}}\right)\right], \tag{B11}$$

where $\hat{t} \equiv \Delta T - 2t_c + 1$. For a given operator $\mathcal{O}_i$ and value of t_c we then jointly fit the correlation functions and $C_{PP}^{SL}(t)$, $C_{PA}^{SL}(t), C_{PP}^{SS}(t)$ and ratios $r^i(t_c, \Delta T)$ (and the LL equivalent for F1M). The fit ranges of $t \in [t_{\min}^{2\text{pt}}, t_{\max}^{2\text{pt}}]$ and $\Delta T \in [\Delta T_{\min}^{3\text{pt}}, \Delta T_{\max}^{3\text{pt}}]$ are chosen such that all fit parameters remain stable when these ranges are varied by small amounts.

APPENDIX C: RENORMALIZATION FACTORS

1. Definitions

We closely follow Ref. [32] in which the reader will find more details. The renormalization factors are defined by imposing the renormalization condition that the projected renormalized amputated-vertex Green's function, in the Landau gauge, for some chosen external momenta, is equal to its tree level value (denoted by F). Using the SMOM kinematics

$$(p_1 - p_2)^2 = p_1^2 = p_2^2 = \mu^2, \tag{C1}$$

the Z-factors are defined in the massless limit ($m_q \to 0$) and extracted by imposing

$$\lim_{m_q \to 0} P_k\left[\frac{Z_{ij}^{\text{RI-SMOM}}(\mu, a)}{(Z_q^{\text{RI-SMOM}}(\mu, a))^2}\Pi_j^{\text{bare}}(a, p_1, p_2)\right]_{\text{SMOM}} = P_k[\Pi_i^{(0)}], \tag{C2}$$

and the tree-level value $F_{ik} \equiv P_k[\Pi_i^{(0)}]$ is obtained by replacing the propagators by the identity in color-Dirac space. Explicitly, for a given four-quark operator Q_i, the vertex functions is defined as (with $\tilde{x}_i = x_i - x$)

$$\Pi_i^{\text{bare}}(a, p_1, p_2)^{\bar{\delta}\bar{\gamma};\bar{\beta}\bar{\alpha}} = \langle \bar{G}(p_2)^{-1}\rangle^{\bar{\delta}\delta}\langle G(p_1)^{-1}\rangle^{\gamma\bar{\gamma}}\langle \bar{G}(p_2)^{-1}\rangle^{\bar{\beta}\beta}\langle G(p_1)^{-1}\rangle^{\alpha\bar{\alpha}}(M_i^{\text{bare}})^{\delta\gamma;\beta\alpha}(a, p_1, p_2), \tag{C3}$$

where

$$(M_i^{\text{bare}})^{\delta\gamma;\beta\alpha}(q^2) = \sum_{x, x_1, \ldots, x_4}\langle 0|s^\delta(x_4)\bar{d}^\gamma(x_3)[Q_i(x)]s^\beta(x_2)\bar{d}^\alpha(x_1)|0\rangle e^{-ip_1\cdot\tilde{x}_1 + ip_2\cdot\tilde{x}_2 - ip_1\cdot\tilde{x}_3 + ip_2\cdot\tilde{x}_4},$$

$$= 2\sum_x(\langle [\bar{G}_x(p_2)\Gamma^1 G_x(p_1)]^{\delta\gamma}[\bar{G}_x(p_2)\Gamma^2 G_x(p_1)]^{\beta\alpha}\rangle - \langle [\bar{G}_x(p_2)\Gamma^1 G_x(p_1)]^{\delta\alpha}[\bar{G}_x(p_2)\Gamma^2 G_x(p_1)]^{\beta\gamma}\rangle). \tag{C4}$$

Here $G_x(p)$ represents an incoming quark with momentum p and $\bar{G}_x(-p)$ an outgoing quark with momentum p. In addition we have also introduced the inverse of the "full momentum" propagators

$$G(p) = \sum_x G_x(p) \quad \text{and} \quad \bar{G}(p) = \sum_x \bar{G}_x(p). \tag{C5}$$

In Eq. (C4), the Dirac structure of the four-quark operator Q_i is encoded in $\Gamma^1 \times \Gamma^2$.

In this work we use two different sets of projectors, $P^{(\gamma_\mu)}$ and $P^{(\not{q})}$, as defined in Ref. [32]. The $P^{(\gamma_\mu)}$ follow the same structure as the four-quark operators. We split them in three groups according to their chiral-flavor properties. For the standard model, we have

$$[P_1^{(\gamma^\mu)}]_{\beta\alpha;\delta\gamma}^{ba;dc} = [(\gamma^\mu)_{\beta\alpha}(\gamma^\mu)_{\delta\gamma} + (\gamma^\mu\gamma^5)_{\beta\alpha}(\gamma^\mu\gamma^5)_{\delta\gamma}]\delta^{ba}\delta^{dc}. \tag{C6}$$

For the (8, 8) doublet we define

$$[P_2^{(\gamma^\mu)}]_{\beta\alpha;\delta\gamma}^{ba;dc} = [(\gamma^\mu)_{\beta\alpha}(\gamma^\mu)_{\delta\gamma} - (\gamma^\mu\gamma^5)_{\beta\alpha}(\gamma^\mu\gamma^5)_{\delta\gamma}]\delta^{ba}\delta^{dc},$$

$$[P_3^{(\gamma^\mu)}]_{\beta\alpha;\delta\gamma}^{ba;dc} = [\delta_{\beta\alpha}\delta_{\delta\gamma} - (\gamma^5)_{\beta\alpha}(\gamma^5)_{\delta\gamma}]\delta^{ba}\delta^{dc}, \tag{C7}$$

and similarly for the $(\bar{6}, 6)$:

$$[P_4^{(\gamma^\mu)}]_{\beta\alpha;\delta\gamma}^{ba;dc} = [\delta_{\beta\alpha}\delta_{\delta\gamma} + (\gamma^5)_{\beta\alpha}(\gamma^5)_{\delta\gamma}]\delta^{ba}\delta^{dc},$$

$$[P_5^{(\gamma^\mu)}]_{\beta\alpha;\delta\gamma}^{ba;dc} = \left[\sum_{\nu>\mu}(\gamma^\mu\gamma^\nu)_{\beta\alpha}(\gamma^\mu\gamma^\nu)_{\delta\gamma}\right]\delta^{ba}\delta^{dc}. \qquad (C8)$$

To define the $P^{(\slashed{q})}$ projectors we replace γ_μ by $\slashed{q}/q^2$ in the previous equations [6]. When there is no explicit γ_μ, we take advantage of some Fierz identities, which relate the color-unmixed four-quark operators of certain Dirac structure to color-mixed four-quark operators of a different Dirac structure [92]. Following Refs. [33,93] we define

$$[P_1^{(\slashed{q})}]_{\beta\alpha;\delta\gamma}^{ba;dc} = \frac{1}{q^2}[(\slashed{q})_{\beta\alpha}(\slashed{q})_{\delta\gamma} + (\slashed{q}\gamma^5)_{\beta\alpha}(\slashed{q}\gamma^5)_{\delta\gamma}]\delta^{ba}\delta^{dc},$$

$$[P_2^{(\slashed{q})}]_{\beta\alpha;\delta\gamma}^{ba;dc} = \frac{1}{q^2}[(\slashed{q})_{\beta\alpha}(\slashed{q})_{\delta\gamma} - (\slashed{q}\gamma^5)_{\beta\delta}(\slashed{q}\gamma^5)_{\delta\gamma}]\delta^{ba}\delta^{dc},$$

$$[P_3^{(\slashed{q})}]_{\beta\alpha;\delta\gamma}^{ba;dc} = \frac{1}{q^2}[(\slashed{q})_{\beta\alpha}(\slashed{q})_{\delta\gamma} - (\slashed{q}\gamma^5)_{\beta\delta}(\slashed{q}\gamma^5)_{\delta\gamma}]\delta^{bc}\delta^{da}.$$

$$[P_4^{(\slashed{q})}]_{\beta\alpha;\delta\gamma}^{ba;dc} = \frac{1}{p_1^2 p_2^2 - (p_1\cdot p_2)^2}[(p_1^\mu(\sigma^{\mu\nu}P_L)p_2^\nu)_{\beta\alpha}(p_1^\rho(\sigma^{\rho\sigma}P_L)p_2^\sigma)_{\delta\gamma}]\delta^{bc}\delta^{da},$$

$$[P_5^{(\slashed{q})}]_{\beta\alpha;\delta\gamma}^{ba;dc} = \frac{1}{p_1^2 p_2^2 - (p_1\cdot p_2)^2}[(p_1^\mu(\sigma^{\mu\nu}P_L)p_2^\nu)_{\beta\alpha}(p_1^\rho(\sigma^{\rho\sigma}P_L)p_2^\sigma)_{\delta\gamma}]\delta^{ba}\delta^{dc}, \qquad (C9)$$

where we used the standard definition $\sigma^{\mu\nu} = \frac{1}{2}[\gamma^\mu, \gamma^\nu]$.

In order to eliminate the explicit Z_q-dependence in Eq. (C2), it is customary to divide the (amputated-projected) vertex function of the four-quark operators by the one of a bilinear operator. Here we choose the axial-vector current and we denote Π_A, P_A, F_A the corresponding vertex function, projector and tree level value, respectively. Finally, the choice of projectors completes the definition of the nonperturbative scheme. Using $\mathcal{A}$ to indicate γ_μ or $\slashed{q}$ we define the renormalization factors $Z_{ij}^{(\mathcal{A},\mathcal{A})}/Z_A^2$ as[3]

$$\frac{Z_{ij}^{(\mathcal{A},\mathcal{A})}(\mu, a)}{Z_A^2(a)} \times \lim_{m_q \to 0} \frac{P_k^{(\mathcal{A})}[\Pi_j^{\text{bare}}(a, p_1, p_2)]}{(P_A^{(\mathcal{A})}[\Pi_A^{\text{bare}}(a, p_1, p_2)])^2}\bigg|_{\text{SMOM}}$$

$$= \frac{F_{ik}^{(\mathcal{A})}}{(F_A^{(\mathcal{A})})^2}. \qquad (C10)$$

Our conventions are such that from Eq. (C10) we can define $Z_{\mathcal{B}_1} \equiv Z_{B_K} = Z_{11}/Z_A^2$. Finally, to obtain the bag parameters we also need to renormalize the quark mass. Making use of $Z_m = 1/Z_S$ we impose

$$\frac{Z_A^{(\mathcal{A})}(\mu, a)}{Z_S(\mu, a)} \times \lim_{m_q \to 0} \frac{P_A^{(\mathcal{A})}[\Pi_A^{\text{bare}}(a, p_1, p_2)]}{P_S[\Pi_S^{\text{bare}}(a, p_1, p_2)]}\bigg|_{\text{SMOM}} = \frac{F_A^{(\mathcal{A})}}{F_S}. \qquad (C11)$$

The use of two schemes provides a way of estimating systematic errors in the renormalization by examining the spread of the results. The vertex function's external momenta p_i^μ are chosen to ensure nonexceptional SMOM kinematics given in Eq. (C1). Using a combination of Fourier momenta and partially twisted boundary conditions, the behavior of the renormalization factors as a function of the momentum scale μ is mapped out in the range $\mu \in [2\text{–}3]$ GeV. In the original exceptional kinematics (used in RI-MOM), infrared effects fall only as p^{-2} and pion pole subtraction is required to tame these. Using nonexceptional kinematics (used in RI-SMOM), the infrared effects are far more suppressed falling with p^{-6} as has been shown in Ref. [94]. Alternative renormalization schemes such as the massive RI-SMOM [95,96] and interpolating MOM-schemes [97] are currently being explored by the collaboration. Their application to kaon mixing is left for future studies.

2. Numerical results for the renormalization factors ensemble by ensemble

On each ensemble we simulate the NPR data points at a range of choices for the renormalization scale μ. These are depicted in Fig. 19. We furthermore repeat the simulation at multiple quark masses, in particular at am_l^{sea}, $2am_l^{\text{sea}}$ and
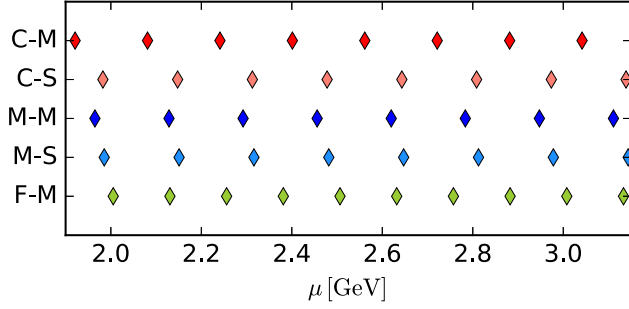
---

[3]We can also define $Z_{ij}^{(\mathcal{A},\mathcal{B})}$ with $\mathcal{A} \neq \mathcal{B}$, but in this work we consider only (γ_μ, γ_μ) and $(\slashed{q}, \slashed{q})$.

FIG. 19. Simulation values of the scale μ on the various ensembles.

$am_s^{\text{sea}}/2$ with the exception of the most expensive C0M and M0M ensembles where we only simulate at $am_s^{\text{sea}}/2$.

We follow the procedure outlined in Appendix C 1 to calculate the four-quark matrix elements' renormalization constants Z_{ij}/Z_A^2. We then normalize these to build the appropriate renormalization constants listed in Eq. (4.3).

In order to ensure reproducibility, we provide numerical values of the renormalization constants at some choice of lattice momenta on the lightest pion mass ensemble for each distinct lattice spacing in Tables XIII–XVII.

3. Extrapolation of the renormalization factors to the massless limit

Formally the renormalization constants are defined in the massless (zero quark mass) limit. In order to perform this limit lattice-spacing-by-lattice-spacing we proceed as follows. We first extrapolate the valence quark mass to zero ensemble-by-ensemble as described in Sec. IV A. We then interpolate the renormalization constants on all ensembles to a fixed scale μ. We either perform a linear fit to the two closest simulated values of μ or a quadratic fit to the three closest points. We then perform a chiral extrapolation in $(am_\pi)^2$ to all ensembles that share an identical lattice spacing (C1S and C2S; C0M and C1M; M1S, M2S and M3S; M0M and M1M). Since we only have data on a single ensemble (F1M) for the finest lattice

TABLE XIII. Values of Z_{ij}/Z_A^2 for chirally nonvanishing matrix elements for a subset of the simulated momenta (in lattice units) on the C0M ensemble for $am_q^{\text{val}} = 0.0181$. All values are given in the RI-SMOM$^{(\gamma_\mu,\gamma_\mu)}$ scheme and in the SUSY basis.

$a\mu$	1.11072	1.3884	1.66608	1.94376
Z_{11}/Z_A^2	0.93224(13)	0.923561(68)	0.915757(54)	0.907465(34)
Z_{22}/Z_A^2	0.74937(13)	0.82424(16)	0.877220(37)	0.917178(57)
Z_{23}/Z_A^2	−0.041062(66)	−0.056518(65)	−0.071844(45)	−0.087583(32)
Z_{32}/Z_A^2	0.03145(13)	−0.010829(52)	−0.043507(40)	−0.071655(36)
Z_{33}/Z_A^2	1.154966(63)	1.106912(37)	1.079801(38)	1.063261(10)
Z_{44}/Z_A^2	0.70331(20)	0.79997(14)	0.867628(12)	0.918149(54)
Z_{45}/Z_A^2	−0.050481(64)	−0.060964(52)	−0.073113(41)	−0.086769(28)
Z_{54}/Z_A^2	−0.171645(50)	−0.149960(37)	−0.139921(39)	−0.137573(37)
Z_{55}/Z_A^2	1.051566(66)	1.049023(33)	1.049000(28)	1.050999(11)
Z_A/Z_S	1.197636(71)	1.129805(84)	1.088466(26)	1.061227(33)

TABLE XIV. Same as Table XIII but for the C1S ensemble for $am_q^{\text{val}} = 0.005$.

$a\mu$	1.11072	1.3884	1.66608	1.94376
Z_{11}/Z_A^2	0.93303(13)	0.924165(55)	0.916271(66)	0.907958(58)
Z_{22}/Z_A^2	0.75249(61)	0.82630(28)	0.87856(11)	0.91832(12)
Z_{23}/Z_A^2	−0.04129(15)	−0.056775(74)	−0.071886(82)	−0.087656(88)
Z_{32}/Z_A^2	0.03059(21)	−0.01137(10)	−0.043656(74)	−0.071733(95)
Z_{33}/Z_A^2	1.15504(28)	1.10673(11)	1.079562(84)	1.063174(48)
Z_{44}/Z_A^2	0.70746(75)	0.80253(30)	0.86921(11)	0.91939(13)
Z_{45}/Z_A^2	−0.05062(20)	−0.06120(10)	−0.073071(83)	−0.086787(86)
Z_{54}/Z_A^2	−0.17065(21)	−0.149293(88)	−0.139280(88)	−0.137090(68)
Z_{55}/Z_A^2	1.05273(21)	1.049571(82)	1.049163(54)	1.051141(43)
Z_A/Z_S	1.19361(86)	1.12820(21)	1.08753(10)	1.060548(76)

TABLE XV.   Same as Table XIII but for the M0M ensemble for $am_q^{\text{val}} = 0.0133$.

$a\mu$	0.83304	1.0413	1.24956	1.3884
Z_{11}/Z_A^2	0.958988(97)	0.948999(54)	0.941580(40)	0.937357(31)
Z_{22}/Z_A^2	0.701561(98)	0.774046(79)	0.826662(61)	0.854299(47)
Z_{23}/Z_A^2	−0.023850(59)	−0.034541(40)	−0.044346(40)	−0.050758(38)
Z_{32}/Z_A^2	0.075307(47)	0.034965(33)	0.005582(30)	−0.010480(23)
Z_{33}/Z_A^2	1.212886(87)	1.149630(45)	1.111072(35)	1.093473(27)
Z_{44}/Z_A^2	0.63286(11)	0.727410(91)	0.796468(58)	0.832571(45)
Z_{45}/Z_A^2	−0.038240(46)	−0.043612(32)	−0.049903(29)	−0.054545(30)
Z_{54}/Z_A^2	−0.182166(54)	−0.154917(30)	−0.137278(21)	−0.129566(23)
Z_{55}/Z_A^2	1.057128(68)	1.050256(31)	1.045950(24)	1.044326(22)
Z_A/Z_S	1.26232(13)	1.181992(83)	1.131563(41)	1.107811(22)

TABLE XVI.   Same as Table XIII but for the M1S ensemble for $am_q^{\text{val}} = 0.004$.

$a\mu$	0.83304	1.0413	1.24956	1.45782
Z_{11}/Z_A^2	0.95866(27)	0.94835(17)	0.94111(13)	0.93495(10)
Z_{22}/Z_A^2	0.70006(63)	0.77412(33)	0.82662(14)	0.86644(13)
Z_{23}/Z_A^2	−0.02394(22)	−0.034736(81)	−0.044604(78)	−0.054232(65)
Z_{32}/Z_A^2	0.07552(21)	0.03452(10)	0.005247(63)	−0.018170(55)
Z_{33}/Z_A^2	1.21448(44)	1.14967(17)	1.111076(76)	1.086321(33)
Z_{44}/Z_A^2	0.63178(68)	0.72810(36)	0.79677(14)	0.84859(14)
Z_{45}/Z_A^2	−0.03853(25)	−0.043920(89)	−0.050118(52)	−0.057240(60)
Z_{54}/Z_A^2	−0.18333(20)	−0.15511(13)	−0.137472(66)	−0.126927(60)
Z_{55}/Z_A^2	1.05863(24)	1.05060(10)	1.046175(54)	1.044027(36)
Z_A/Z_S	1.2629(14)	1.18148(46)	1.13157(10)	1.09803(10)

TABLE XVII.   Same as Table XIII but for the F1M ensemble for $am_q^{\text{val}} = 0.0021$.

$a\mu$	0.74048	0.87932	1.01816	1.43468
Z_{11}/Z_A^2	0.97098(29)	0.96182(11)	0.955127(87)	0.941078(33)
Z_{22}/Z_A^2	1.06173(45)	1.05453(10)	1.049270(35)	1.041636(15)
Z_{23}/Z_A^2	0.37422(52)	0.32971(35)	0.29528(14)	0.239419(67)
Z_{32}/Z_A^2	0.01748(19)	0.018812(88)	0.020455(43)	0.026601(18)
Z_{33}/Z_A^2	0.61015(69)	0.68079(75)	0.73890(33)	0.85407(11)
Z_{44}/Z_A^2	0.69653(77)	0.75380(76)	0.80124(37)	0.89759(12)
Z_{45}/Z_A^2	−0.00933(14)	−0.01280(13)	−0.015992(62)	−0.025037(17)
Z_{54}/Z_A^2	−0.36177(54)	−0.31116(28)	−0.27401(16)	−0.215021(71)
Z_{55}/Z_A^2	1.23079(76)	1.17174(16)	1.130128(97)	1.058518(33)
Z_A/Z_S	1.28592(66)	1.22090(96)	1.17291(37)	1.093643(58)

spacing, we apply each of the slopes with m_π^2 in turn. On F-M, we assign the central value to be the mean of these four extrapolated results and take half the spread of the results as a systematic uncertainty associated to the chiral extrapolation. We provide numerical values of these chirally extrapolated renormalization constants for each of the lattice spacings at $\mu = 2$ GeV (Table VI), $\mu = 2.5$ GeV (Table XVIII), and $\mu = 3$ GeV (Table XIX).

TABLE XVIII.   Same as Table VI but at mass scale $\mu = 2.5$ GeV.

a^{-1} [GeV]	1.7295(38)	1.7848(50)	2.3586(70)	2.3833(86)	2.708(10)
Z_{11}/Z_A^2	0.92273(29)(1)	0.92491(52)(0)	0.94913(20)(0)	0.94752(86)(2)	0.95950(43)(33)
Z_{22}/Z_S^2	1.05048(77)(4)	1.0519(13)(0)	1.08128(96)(1)	1.0830(21)(0)	1.0964(11)(6)
Z_{23}/Z_S^2	−0.07511(48)(3)	−0.07280(82)(2)	−0.04932(29)(0)	−0.04900(66)(1)	−0.04007(40)(17)
Z_{32}/Z_S^2	−0.0228(16)(1)	−0.0162(45)(0)	0.0447(28)(1)	0.0465(63)(1)	0.0746(37)(0)
Z_{33}/Z_S^2	1.3816(30)(7)	1.4014(83)(2)	1.5913(50)(6)	1.603(11)(0)	1.6981(67)(17)
Z_{44}/Z_S^2	1.02458(44)(3)	1.02303(97)(4)	1.01873(49)(7)	1.0201(14)(0)	1.01595(76)(71)
Z_{45}/Z_S^2	−0.07967(51)(2)	−0.07835(69)(1)	−0.06134(25)(1)	−0.06193(46)(0)	−0.05599(23)(24)
Z_{54}/Z_S^2	−0.18458(58)(19)	−0.1880(18)(0)	−0.2130(11)(1)	−0.2162(26)(1)	−0.2305(15)(5)
Z_{55}/Z_S^2	1.3170(21)(5)	1.3310(60)(1)	1.4581(36)(3)	1.4673(80)(5)	1.5267(46)(17)

TABLE XIX.   Same as Table VI but at mass scale $\mu = 3.0$ GeV.

a^{-1} [GeV]	1.7295(38)	1.7848(50)	2.3586(70)	2.3833(86)	2.708(10)
Z_{11}/Z_A^2	0.91427(17)(0)	0.91641(55)(0)	0.94123(17)(1)	0.94044(67)(0)	0.95157(31)(27)
Z_{22}/Z_S^2	1.03795(18)(4)	1.03874(73)(2)	1.05744(45)(5)	1.0596(10)(0)	1.06947(54)(36)
Z_{23}/Z_S^2	−0.08818(26)(2)	−0.08564(98)(0)	−0.05786(22)(0)	−0.05804(54)(0)	−0.04741(25)(25)
Z_{32}/Z_S^2	−0.0589(10)(0)	−0.0532(31)(0)	0.0036(18)(0)	0.0052(44)(0)	0.0300(24)(1)
Z_{33}/Z_S^2	1.2568(19)(2)	1.2711(59)(2)	1.4093(34)(4)	1.4206(79)(1)	1.4919(44)(11)
Z_{44}/Z_S^2	1.03009(18)(0)	1.02856(45)(0)	1.02098(20)(0)	1.02223(60)(0)	1.01811(29)(38)
Z_{45}/Z_S^2	−0.08895(23)(2)	−0.08683(80)(0)	−0.06453(14)(1)	−0.06486(36)(0)	−0.05716(16)(22)
Z_{54}/Z_S^2	−0.16199(30)(9)	−0.1636(11)(0)	−0.17286(72)(9)	−0.1757(17)(0)	−0.1842(10)(3)
Z_{55}/Z_S^2	1.2268(12)(1)	1.2368(41)(1)	1.3299(24)(2)	1.3389(57)(1)	1.3852(31)(10)

TABLE XX.   Chirally-allowed elements of the nonperturbative scaling matrix $\sigma(3$ GeV, 2 GeV$)$ using chirally extrapolated Z-factors.

a^{-1} [GeV]	1.7848(50)	1.7295(38)	2.3833(86)	2.3586(70)	2.708(10)
σ_{22}	1.1866(15)	1.18862(99)	1.2055(27)	1.1980(16)	1.2047(16)
σ_{23}	−0.020560(36)	−0.02201(14)	−0.01408(33)	−0.01294(22)	−0.01165(18)
σ_{32}	−0.09661(26)	−0.09870(19)	−0.09318(55)	−0.09034(41)	−0.08994(17)
σ_{33}	0.94800(88)	0.95149(38)	0.92958(89)	0.93208(35)	0.92586(49)
σ_{44}	1.2441(30)	1.2447(15)	1.2844(46)	1.2748(21)	1.2910(23)
σ_{45}	−0.00982(21)	−0.01235(22)	−0.00146(54)	−0.00159(23)	0.00067(30)
σ_{54}	0.0439(12)	0.04063(45)	0.0711(17)	0.06801(83)	0.0774(10)
σ_{55}	1.017341(75)	1.018409(16)	1.00827(44)	1.00994(39)	1.00838(48)

4. Step-scaling matrices

We choose a lower scale μ for nonperturbative renormalization to reduce cutoff effects, and a higher scale μ' for matching to $\overline{\text{MS}}$. This distance is bridged using nonperturbative running

$$O_i^{\overline{\text{MS}}}(\mu') = R_{ij}^{\overline{\text{MS}}\leftarrow\text{RI}}(\mu')\sigma_{jk}(\mu',\mu)O_k^{\text{RI}}(\mu), \quad \text{(C12)}$$

O_i being any of the quantities in Eq. (4.3). The matching factors $R_{ij}^{\overline{\text{MS}}\leftarrow\text{RI}}$ are computed in next-to-leading order perturbation theory and presented in Ref. [33] for both schemes. The nonperturbative scale evolution matrix is given by

$$\sigma_{ij}(\mu',\mu) = \lim_{a\to 0}\sigma_{ij}(\mu',\mu,a)$$
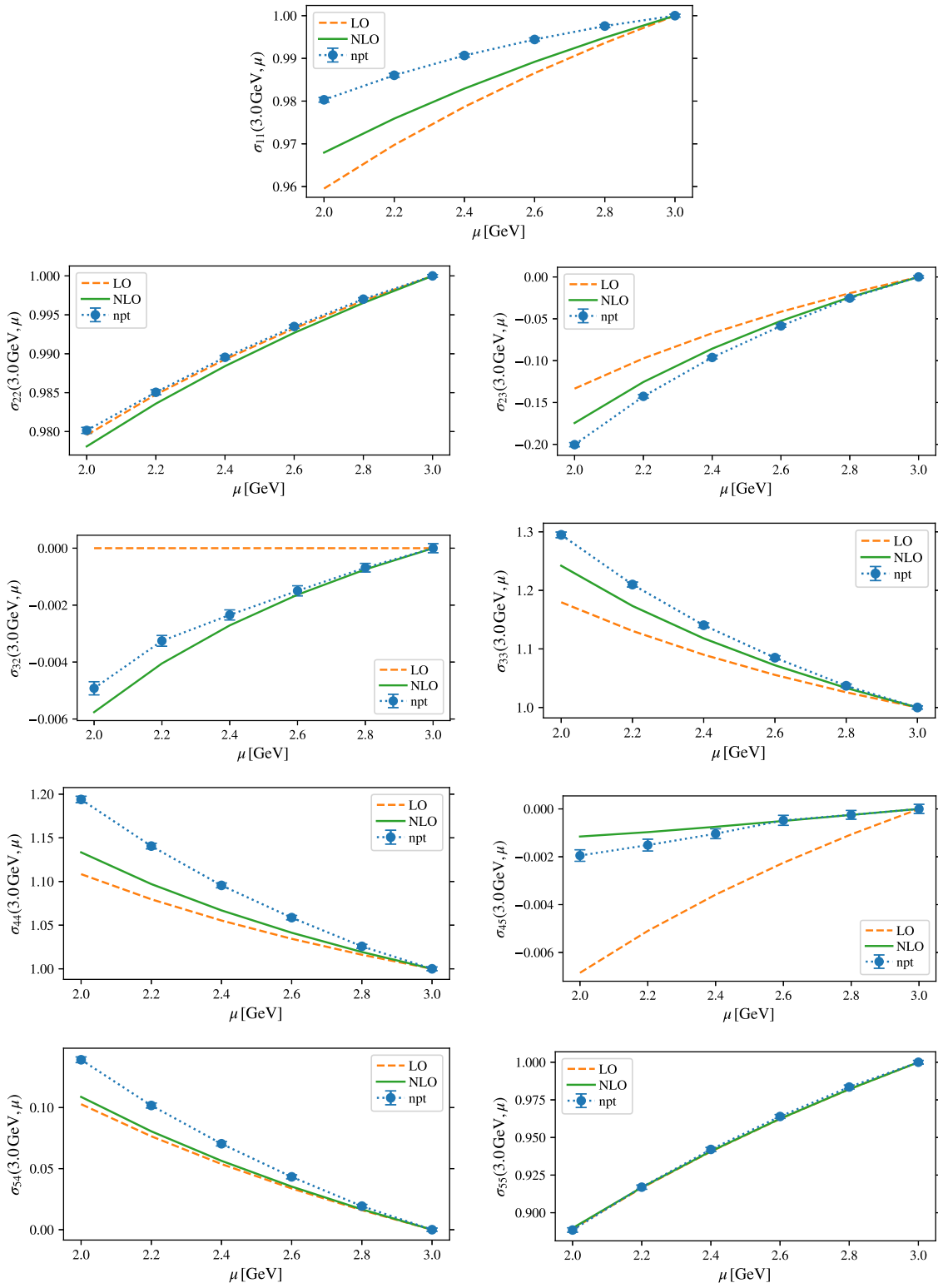$$= \lim_{a\to 0}Z_{ik}(\mu',a)Z_{kj}(\mu,a)^{-1}. \quad \text{(C13)}$$

FIG. 20. Comparison of the scale evolution matrix $\sigma(3\text{ GeV}, \mu)$ [see Eq. (4.4)] in the RI-SMOM$^{(\gamma_\mu, \gamma_\mu)}$ scheme and NPR basis evaluated nonperturbatively (blue circles), perturbatively at leading order (orange dashed lines) and next-to-leading order (green solid lines).

We perform this continuum limit including the chirally extrapolated renormalization constants (numerical values listed in Table XX) from all lattice spacings as a fit linear in a^2. In the few cases where the quality of fit does not lead to an acceptable p-value, we rescale the uncertainty by $\sqrt{\chi^2/\text{d.o.f.}}$. In Fig. 20 we compare our nonperturbative step-scaling results to leading and next-to-leading order perturbation theory. For completeness we also provide the step-scaling matrices, σ_R, for the R_i

$$
\sigma_R(3 \text{ GeV}, 2 \text{ GeV}) =
\begin{bmatrix}
1.0 & 0.0 & 0.0 & 0.0 & 0.0 \\
0.0 & 1.2153(28) & -0.08396(60) & 0.0 & 0.0 \\
0.0 & -0.00426(52) & 0.90868(42) & 0.0 & 0.0 \\
0.0 & 0.0 & 0.0 & 1.3186(42) & 0.1018(15) \\
0.0 & 0.0 & 0.0 & 0.00976(68) & 0.99984(59)
\end{bmatrix},
\tag{C14}
$$

$$
\sigma_R(3 \text{ GeV} \xleftarrow{\Delta=0.5} 2 \text{ GeV}) =
\begin{bmatrix}
1.0 & 0.0 & 0.0 & 0.0 & 0.0 \\
0.0 & 1.2149(25) & -0.08315(50) & 0.0 & 0.0 \\
0.0 & -0.00374(43) & 0.90889(40) & 0.0 & 0.0 \\
0.0 & 0.0 & 0.0 & 1.3190(35) & 0.1023(14) \\
0.0 & 0.0 & 0.0 & 0.01083(44) & 0.99940(59)
\end{bmatrix}.
\tag{C15}
$$

APPENDIX D: RELATIONS BETWEEN BASIS CONVENTIONS

We distinguish between operators O_i in the "SUSY" basis, defined in Eq. (2.2), and operators Q_i in the "NPR" or "lattice" basis, in Eq. (2.4). The SUSY basis contains both color-unmixed and color-mixed operators, while the NPR basis comprises only color-unmixed operators, more convenient for lattice computations. For the $K^0\bar{K}^0$ matrix elements of these operators we need only the parity-even parts, O_i^+ or Q_i^+, shown in Eqs. (2.3) and (2.5). Since we work with the Q_i^+ on the lattice, we quote here the matrix T which relates the Q_i^+ to the O_i^+

$$
O^+ = TQ^+ =
\begin{pmatrix}
1 & 0 & 0 & 0 & 0 \\
0 & 0 & 0 & 1 & 0 \\
0 & 0 & 0 & -\frac{1}{2} & \frac{1}{2} \\
0 & 0 & 1 & 0 & 0 \\
0 & -\frac{1}{2} & 0 & 0 & 0
\end{pmatrix} Q^+
\quad \text{or} \quad
\begin{pmatrix}
O_1^+ \\
O_2^+ \\
O_3^+ \\
O_4^+ \\
O_5^+
\end{pmatrix}
=
\begin{pmatrix}
Q_1^+ \\
Q_4^+ \\
(Q_5^+ - Q_4^+)/2 \\
Q_3^+ \\
-Q_2^+/2
\end{pmatrix}.
\tag{D1}
$$

We perform our nonperturbative calculations of the matrix elements and renormalization constants in the NPR basis and subsequently convert to the SUSY basis. Matrix elements of the renormalized Q_i^+ in some scheme X at scale μ are given by,

$$
\langle K|Q_i^+|\bar{K}\rangle^X(\mu) = Z_{ij}^X(\mu)\langle K|Q_{j,\text{bare}}^+|\bar{K}\rangle.
\tag{D2}
$$

When chiral symmetry is maintained, $Z_{ij}^X(\mu)$ is block-diagonal and the matrix elements of the renormalized operators O_i^+ in the SUSY basis in scheme X at scale μ are related to matrix elements of the bare operators in the NPR basis by,

$$
\begin{pmatrix}
\langle K|O_1^+|\bar{K}\rangle \\
\langle K|O_2^+|\bar{K}\rangle \\
\langle K|O_3^+|\bar{K}\rangle \\
\langle K|O_4^+|\bar{K}\rangle \\
\langle K|O_5^+|\bar{K}\rangle
\end{pmatrix}
=
\begin{pmatrix}
Z_{11}^X & 0 & 0 & 0 & 0 \\
0 & 0 & 0 & Z_{44}^X & Z_{45}^X \\
0 & 0 & 0 & \frac{-Z_{44}^X+Z_{54}^X}{2} & \frac{-Z_{45}^X+Z_{55}^X}{2} \\
0 & Z_{32}^X & Z_{33}^X & 0 & 0 \\
0 & -\frac{Z_{22}^X}{2} & -\frac{Z_{23}^X}{2} & 0 & 0
\end{pmatrix}
\begin{pmatrix}
\langle K|Q_{1,\text{bare}}^+|\bar{K}\rangle \\
\langle K|Q_{2,\text{bare}}^+|\bar{K}\rangle \\
\langle K|Q_{3,\text{bare}}^+|\bar{K}\rangle \\
\langle K|Q_{4,\text{bare}}^+|\bar{K}\rangle \\
\langle K|Q_{5,\text{bare}}^+|\bar{K}\rangle
\end{pmatrix}.
\tag{D3}
$$

The NPR-basis operators are written in color-unmixed form. They are related by Fierz transformations to the same operators written in color-mixed form by $Q_i^{\text{mix}} = F_{ij}Q_j^{\text{unmixed}}$, where

$$F = \begin{pmatrix} 1 & 0 & 0 & 0 & 0 \\ 0 & 0 & -2 & 0 & 0 \\ 0 & -\frac{1}{2} & 0 & 0 & 0 \\ 0 & 0 & 0 & -\frac{1}{2} & \frac{1}{2} \\ 0 & 0 & 0 & \frac{3}{2} & \frac{1}{2} \end{pmatrix}. \quad \text{(D4)}$$

The matrix F is used when working out the matrix T which transforms from the NPR basis to the SUSY basis.

APPENDIX E: PERTURBATIVE SCALING

We compare our nonperturbative scaling results with perturbation theory in Fig. 20 and hence include here our notation and definitions for the perturbative computations to next-to-leading order. Full details are provided in a *Mathematica* [98] notebook as Supplemental Material . This is well-covered ground [99–102], but by explicitly including both g^2 and $g^2 \log(g)$ terms at NLO we are able to avoid having to take a limit to compute the scaling matrix at NLO.

The (matrix) operator renormalization constants and scaling matrix are related by

$$Z(\mu') = \sigma(\mu', \mu)Z(\mu). \quad \text{(E1)}$$

The anomalous dimension matrix, γ is defined by

$$\mu \frac{dZ}{d\mu} = -\gamma Z. \quad \text{(E2)}$$

Using $\mu dg/d\mu = \beta(g)$, we have

$$\sigma(\mu', \mu) = \text{T}_g \exp\left(\int_{g(\mu)}^{g(\mu')} dg' \frac{-\gamma(g)}{\beta(g)} \right), \quad \text{(E3)}$$

where T_g denotes g-ordering. We let

$$\bar{a} = \frac{\alpha}{4\pi} = \frac{g^2}{16\pi^2} \quad \text{(E4)}$$

and expand

$$\begin{aligned} \beta(g) &= -\beta^0 g\bar{a} - \beta^1 g\bar{a}^2 + \cdots \\ \gamma(g) &= \gamma^0 \bar{a} + \gamma^1 \bar{a}^2 + \cdots \end{aligned} \quad \text{(E5)}$$

so that

$$\int_{g(\mu)}^{g(\mu')} dg' \frac{-\gamma(g')}{\beta(g')} = \int_{\bar{a}(\mu)}^{\bar{a}(\mu')} \frac{d\bar{a}'}{\bar{a}'} \frac{(\gamma^0 + \gamma^1 \bar{a}' + \cdots)}{2(\beta^0 + \beta^1 \bar{a}' + \cdots)}. \quad \text{(E6)}$$

With our conventions, $\beta^0 = 11 - 2N_f/3$ for N_f flavors. We work with the operators Q_i^+ defined in Eq. (2.5). They are related to the positive parity parts of the basis $Q_{\text{BMU}} = \{Q_1^{\text{VLL}}, Q_1^{\text{LR}}, Q_2^{\text{LR}}, Q_1^{\text{SLL}}, Q_2^{\text{SLL}}\}$ used in Ref. [100] by $Q^+ = R \cdot Q_{\text{BMU}}^+$ with $R = \text{diag}(4, 4, 4, 4, 1)$. This changes the off-diagonal elements of the anomalous dimension matrices in the bottom-right 2×2 block. In Ref. [102], the anomalous dimension is defined with the opposite sign and expanded as $\gamma^{\text{PPP}} = -g^2(\gamma^{0,\text{PPP}} + \gamma^{1,\text{PPP}}g^2 + \cdots)$, which means that $\gamma^{0,\text{PPP}} = \gamma^0/(16\pi^2)$.

1. LO scaling

If we diagonalize γ^0,

$$V^{-1}\gamma^0 V = \gamma_D^0, \quad \text{(E7)}$$

where γ_D^0 is the diagonal matrix of eigenvalues, then the scaling matrix at leading order is

$$\sigma^0(\mu', \mu) = V \left(\frac{a(\mu')}{a(\mu)} \right)^{\gamma_D^0/2\beta^0} V^{-1}. \quad \text{(E8)}$$

To match notation from Ref. [100], we write

$$(V^{-1}\gamma^0 V)_{ij} = 2\beta^0 a_i \delta_{ij} \quad \text{where} \quad a = \frac{\gamma_D^0}{2\beta^0}. \quad \text{(E9)}$$

Under $\text{SU}(3)_L \times \text{SU}(3)_R$ flavor, Q_1^+ is (27, 1) and renormalizes multiplicatively, $Q_{2,3}^+$ are (8, 8) and mix, and $Q_{4,5}^+$ are $(6, \bar{6})$ and also mix. When we diagonalize γ^0 we permute the eigenvalues and eigenvectors to preserve the block-diagonal structure of the 5×5 anomalous dimension matrix. Our choice leads to

$$\gamma_D^0 = \text{diag}\left(4, 2, -16, \frac{2}{3}(1 + \sqrt{241}), \frac{2}{3}(1 - \sqrt{241})\right). \quad \text{(E10)}$$

2. NLO scaling

Beyond leading order we write

$$\sigma(\mu', \mu) \equiv K(\mu')\sigma^0(\mu', \mu)K^{-1}(\mu). \quad \text{(E11)}$$

The equation satisfied by K is

$$\frac{\partial K}{\partial g} - \frac{1}{g}\left[\frac{\gamma^0}{\beta^0}, K\right] = -\left(\frac{\gamma(g)}{\beta(g)} + \frac{\gamma^0}{\beta^0 g}\right)K, \quad \text{(E12)}$$

where $K = K(\mu)$ and $g = g(\mu)$. Expanding to NLO in the coupling and writing

$$K = 1 + \frac{g^2}{16\pi^2}J + \frac{g^2}{16\pi^2}\log(g)L, \qquad \text{(E13)}$$

we find that J and L satisfy

$$L = \left[\frac{\gamma^0}{2\beta^0}, L\right]$$

$$J + \frac{1}{2}L = \left[\frac{\gamma^0}{2\beta^0}, J\right] + \frac{1}{2\beta^0}\gamma^1 - \frac{\beta^1}{2(\beta^0)^2}\gamma^0. \qquad \text{(E14)}$$

Using the matrix V from Eq. (E7) which diagonalizes γ^0, we define

$$G = V^{-1}\gamma^1 V$$
$$S = V^{-1}JV$$
$$T = V^{-1}LV \qquad \text{(E15)}$$

and recalling the a_i from Eq. (E9), we find

$$T_{ij} = (a_i - a_j)T_{ij}. \qquad \text{(E16)}$$

This shows that T_{ij} vanishes, *except* when $a_i - a_j = 1$. We also have

$$S_{ij} + \frac{1}{2}T_{ij} - (a_i - a_j)S_{ij} = \frac{1}{2\beta^0}G_{ij} - \frac{\beta^1}{\beta^0}a_i\delta_{ij}. \qquad \text{(E17)}$$

If $a_i - a_j = 1$ then S_{ij} drops out of this equation and its value is arbitrary (we choose to make it zero), but then T_{ij} is nonzero from the previous equation and its value is determined by this equation. If $a_i - a_j \neq 1$, then $T_{ij} = 0$ and the equation determines S_{ij}. Once we know S and T we can find J and L and hence determine the K matrix and the NLO expression for the scaling matrix σ.

The leading order anomalous dimension matrix for the 4-quark operators has $a_2 - a_3 = 1$ when the number of flavors is $N_f = 3$. This means that $T_{23} \neq 0$ and there is a $g^2 \log g$ term in K_{23}. Including the $g^2 \log g$ term allows us to avoid expanding the solution for the scaling matrix around $N_f = 3$. We checked that either method gives the same result for σ. For our check we shifted $a_2 \to a_2 + \delta$, computed the scaling matrix σ and took the limit $\delta \to 0$. As an additional check we also did the limiting procedure by shifting $\beta^0 \to 11 - 2(3 + \delta)/3$ when constructing $a = \gamma_D^0/2\beta^0$ in Eq. (E9) and again found the same result. We also learn and checked that we can add an arbitrary shift to S_{23} or J_{23} without changing the result for σ.

From Eq. (E14) we know that the only nonzero element of T in any scheme is $T_{23} = G_{23}/\beta^0$ and hence in any scheme,

$$L_{23} = \frac{(V^{-1}\gamma^1 V)_{23}}{\beta^0(V^{-1})_{22}V_{33}} = -\frac{40}{27} = -1.48148. \qquad \text{(E18)}$$

We checked this for $\overline{\text{MS}}$, RI-MOM, RI-SMOM$^{(\gamma_\mu,\gamma_\mu)}$ and RI-SMOM$^{(\slashed{q},\slashed{q})}$.

For γ^1 in $\overline{\text{MS}}$ we used Ref. [100] and for RI-MOM we used Ref. [102] (that paper does not give the 11 element; for this we used the value in Ref. [6]). For the RI-SMOM schemes we used $\gamma^{\overline{\text{MS}},1}$ together with the conversion factors Δr from RI-SMOM to $\overline{\text{MS}}$ in Ref. [33] and applied Eq. (E27) below.

To evaluate the perturbative scaling numerically, we used the 5-loop expression for the running strong coupling to evolve its value from the Z-mass to the charm mass, with quark-flavor thresholds at $\bar{m}_b(\bar{m}_b)$ and $\bar{m}_c(\bar{m}_c)$, the $\overline{\text{MS}}$ bottom and charm masses evaluated at their own scales [103–114]. We then evaluated $\alpha_s(\mu)$ for $2 \text{ GeV} \leq \mu \leq 3 \text{ GeV}$ for three flavors, corresponding to our $2 + 1$ flavor simulations. Our inputs were [62]

$$\alpha_s(M_Z) = 0.1180,$$
$$M_Z = 91.1876 \text{ GeV},$$
$$\bar{m}_b(\bar{m}_b) = 4.18 \text{ GeV},$$
$$\bar{m}_c(\bar{m}_c) = 1.28 \text{ GeV}, \qquad \text{(E19)}$$

and we determine

$$\alpha_s(2 \text{ GeV}) = 0.293347, \quad \alpha_s(3 \text{ GeV}) = 0.243580. \qquad \text{(E20)}$$

Changing from operators $Q^+(\mu)$ renormalized in some scheme at scale μ to RGI operators $\hat{Q}^+$, is done by [102]:

$$\hat{Q}^+ = [\alpha(\mu)]^{-\gamma^0/2\beta^0}K^{-1}(\mu)Q^+(\mu). \qquad \text{(E21)}$$

The 11 element of this relation converts the kaon bag parameter $B_K(\mu)$ to the RGI $\hat{B}_K$ (see for example the discussion in the 2019 FLAG review [115]). To compute RGI $\hat{B}_i$'s for the BSM operators, we would in addition have to take into account the quark-mass combination $m_s(\mu) + m_d(\mu)$ appearing in the $B_i(\mu)$'s definition.

3. Logarithmic term in NLO scaling expression

Here we will let $g' = g(\mu')$, $\alpha' = \alpha(\mu')$ and $g = g(\mu)$, $\alpha = \alpha(\mu)$. From Eqs. (E11) and (E13), the $\log(g)$ terms in $\sigma(\mu',\mu)$ at NLO are

$$\frac{1}{4\pi}(\alpha' \log g' L\sigma^0(\mu',\mu) - \alpha \log g\sigma^0(\mu',\mu)L)$$

$$= \frac{1}{4\pi}V\left(\alpha' \log g' T\left(\frac{\alpha'}{\alpha}\right)^a - \alpha \log g\left(\frac{\alpha'}{\alpha}\right)^a T\right)V^{-1}. \qquad \text{(E22)}$$

From above, the only nonzero element of T is T_{23}, so the term in parentheses becomes

$$T_{23}\left(\alpha' \log g'\left(\frac{\alpha'}{\alpha}\right)^{a_3} - \alpha \log g\left(\frac{\alpha'}{\alpha}\right)^{a_2}\right)$$
$$= T_{23}\left(\frac{\alpha'}{\alpha}\right)^{1/9} \alpha \log\left(\frac{g'}{g}\right) \qquad (E23)$$

where we have used $a_2 = 1/9$ and $a_3 = -8/9$. Switching back to L and expressing everything in terms of α' and α we find

$$\text{NLO logs in } \sigma(\mu',\mu) = -\frac{5}{(27\pi)}\left(\frac{\alpha'}{\alpha}\right)^{1/9} \alpha \log\left(\frac{\alpha'}{\alpha}\right). \qquad (E24)$$

We checked explicitly for $\overline{\text{MS}}$, RI-MOM, RI-SMOM$^{(\gamma_\mu,\gamma_\mu)}$ and RI-SMOM$^{(\not{q},\not{q})}$ that the same term arises when we calculate the NLO scaling by the δ-shift and limit procedure.

4. Scheme conversion

Following Ref. [33] we define the matrix R to convert from renormalization scheme A to scheme B by

$$Z^B = R^{B\leftarrow A} Z^A = (1 - \bar{a}\Delta r^{B\leftarrow A})Z^A, \qquad (E25)$$

where $\bar{a} = g^2/16\pi^2$. From $\beta(g)dZ^B/dg = -\gamma^B(g)Z^B$ we find

$$\gamma^A = (R^{B\leftarrow A})^{-1}\gamma^B R^{B\leftarrow A} + \beta(R^{B\leftarrow A})^{-1}\frac{dR^{B\leftarrow A}}{dg}. \qquad (E26)$$

Expanding to $O(\bar{a}^2)$ and noting that γ^0 is universal, we can relate the NLO anomalous dimensions in schemes A and B using the 1-loop conversion factor $\Delta r^{B\leftarrow A}$,

$$\gamma^{A,1} = \gamma^{B,1} - [\gamma^0, \Delta r^{B\leftarrow A}] + 2\beta^0 \Delta r^{B\leftarrow A}. \qquad (E27)$$

In particular we can determine the NLO anomalous dimensions where A is RI-SMOM$^{(\gamma_\mu,\gamma_\mu)}$ or RI-SMOM$^{(\not{q},\not{q})}$ respectively, from the $\overline{\text{MS}}$ NLO anomalous dimension and $\Delta r^{\overline{\text{MS}}\leftarrow A}$

$$\gamma^{A,1} = \gamma^{\overline{\text{MS}},1} - [\gamma^0, \Delta r^{\overline{\text{MS}}\leftarrow A}] + 2\beta^0 \Delta r^{\overline{\text{MS}}\leftarrow A}. \qquad (E28)$$

By combining the scheme conversion equation (E27) with Eq. (E14) for J and L, we can show that

$$J^A - J^{\overline{\text{MS}}} = \Delta r^{\overline{\text{MS}}\leftarrow A} \quad \text{except for the 23 element} \qquad (E29)$$

and that $L^A = L^{\overline{\text{MS}}}$. We checked Eq. (E29) when A is RI-MOM, RI-SMOM$^{(\gamma_\mu,\gamma_\mu)}$ or RI-SMOM$^{(\not{q},\not{q})}$.

APPENDIX F: FURTHER DETAILED NUMERICAL FIT RESULTS

Our central value for the $\mathcal{B}_i$ and R_i in $\overline{\text{MS}}$ at $\mu = 3$ GeV is taken as the mean of the conversion from RI-SMOM$^{(\gamma_\mu,\gamma_\mu)}$ and RI-SMOM$^{(\not{q},\not{q})}$ to $\overline{\text{MS}}$. For completeness we also separately list these conversions with their full uncertainty budget in Table XXI.

TABLE XXI. Central values and combined systematic errors for ratio and bag parameters at $\mu = 3$ GeV in $\overline{\text{MS}}$ after converting from the two RI-SMOM schemes—(γ_μ, γ_μ) and $(\not{q}, \not{q})$, in the SUSY basis. We list the errors arising from statistics, chiral extrapolation, residual chiral symmetry breaking, and discretization and combine it into total uncertainties.

Scheme		R_2	R_3	R_4	R_5	$\mathcal{B}_1$	$\mathcal{B}_2$	$\mathcal{B}_3$	$\mathcal{B}_4$	$\mathcal{B}_5$
$\overline{\text{MS}} \leftarrow$ RI-SMOM$^{(\gamma_\mu,\gamma_\mu)}$	Central	-18.73	5.781	41.45	10.80	0.5185	0.4759	0.728	0.8862	0.6977
	Statistical	0.60%	0.69%	0.72%	0.43%	0.28%	0.24%	0.72%	0.21%	1.02%
	Chiral	0.21%	0.42%	0.61%	0.46%	0.20%	0.17%	0.29%	0.17%	0.25%
	rcsb	0.10%	0.15%	0.09%	0.03%	0.04%	0.03%	0.06%	0.01%	0.00%
	discr	0.16%	0.53%	0.49%	1.23%	0.01%	0.44%	1.61%	0.16%	0.38%
	Total	0.66%	0.98%	1.07%	1.38%	0.35%	0.53%	1.79%	0.32%	1.12%
$\overline{\text{MS}} \leftarrow$ RI-SMOM$^{(\not{q},\not{q})}$	Central	-19.07	6.059	42.43	10.49	0.5295	0.4829	0.764	0.9070	0.6788
	Statistical	0.68%	0.92%	0.81%	0.83%	0.29%	0.43%	1.24%	0.36%	2.21%
	Chiral	0.48%	0.78%	1.25%	1.26%	0.24%	0.27%	0.44%	0.29%	0.51%
	rcsb	0.29%	0.21%	0.23%	0.13%	0.08%	0.19%	0.29%	0.03%	0.01%
	discr	0.34%	0.65%	0.20%	2.30%	0.10%	0.64%	1.92%	0.19%	0.10%
	Total	0.95%	1.39%	1.52%	2.75%	0.40%	0.83%	2.34%	0.50%	2.27%

[1] J. H. Christenson, J. W. Cronin, V. L. Fitch, and R. Turlay, Evidence for the 2π decay of the k_2^0 meson, Phys. Rev. Lett. **13,** 138 (1964).

[2] Andrzej Buras, *Gauge Theory of Weak Decays* (Cambridge University Press, Cambridge, England, 2020).

[3] Ikaros I. Bigi and A. I. Sanda, *CP Violation* (Cambridge University Press, Cambridge, England, 2009), Vol. 9.

[4] Gustavo C. Branco, Luis Lavoura, and Joao P. Silva, *CP Violation* (Oxford University Press, New York, 1999), Vol. 103.

[5] T. Inami and C. S. Lim, Effects of superheavy quarks and leptons in low-energy weak processes $K_L \to \mu\bar{\mu}, K^+ \to \pi^+\nu\bar{\nu}$, $K^0 \leftrightarrow \bar{K}^0$, Prog. Theor. Phys. **65,** 297 (1981); **65,** 1772(E) (1981).

[6] Y. Aoki, R. Arthur, T. Blum, P. A. Boyle, D. Brommel *et al.*, Continuum limit of B_K from $2 + 1$ flavor domain wall QCD, Phys. Rev. D **84,** 014503 (2011).

[7] T. Blum *et al.* (RBC, UKQCD Collaborations), Domain wall QCD with physical quark masses, Phys. Rev. D **93,** 074505 (2016).

[8] Taegil Bae *et al.* (SWME Collaboration), Neutral kaon mixing from new physics: Matrix elements in $N_f = 2 + 1$ lattice QCD, Phys. Rev. D **88,** 071503 (2013).

[9] Benjamin J. Choi *et al.* (SWME Collaboration), Kaon BSM B-parameters using improved staggered fermions from $N_f = 2 + 1$ unquenched QCD, Phys. Rev. D **93,** 014511 (2016).

[10] Taegil Bae *et al.* (SWME Collaboration), Improved determination of BK with staggered quarks, Phys. Rev. D **89,** 074504 (2014).

[11] N. Carrasco, P. Dimopoulos, R. Frezzotti, V. Lubicz, G. C Rossi, S. Simula, and C. Tarantino (ETM Collaboration), $\Delta S = 2$ and $\Delta C = 2$ bag parameters in the standard model and beyond from $N_f = 2 + 1 + 1$ twisted-mass lattice QCD, Phys. Rev. D **92,** 034516 (2015).

[12] V. Bertone *et al.* (ETM Collaboration), Kaon mixing beyond the SM from $N_f = 2$ tmQCD and model independent constraints from the UTA, J. High Energy Phys. 03 (2013) 089; 07 (2013) 143(E).

[13] Y. Aoki *et al.* (Flavour Lattice Averaging Group (FLAG) Collaboration), FLAG review 2021, Eur. Phys. J. C **82,** 869 (2022).

[14] Gerhard Buchalla, Andrzej J. Buras, and Markus E. Lautenbacher, Weak decays beyond leading logarithms, Rev. Mod. Phys. **68,** 1125 (1996).

[15] Norman H. Christ, Computing the long-distance contribution to the kaon mixing parameter ϵ_K, Proc. Sci. LATTICE2011 (**2011**) 277 [arXiv:1201.2065].

[16] Norman H. Christ and Ziyuan Bai, Computing the long-distance contributions to ε_K, Proc. Sci. LATTICE2015 (**2016**) 342.

[17] Ziyuan Bai, Long distance part of ϵ_K from lattice QCD, Proc. Sci. LATTICE2016 (**2017**) 309 [arXiv:1611.06601].

[18] Bigeng Wang, Calculating Δm_K with lattice QCD, Proc. Sci. LATTICE2021 (**2022**) 141 [arXiv:2301.01387].

[19] Ziyuan Bai, Norman H. Christ, Joseph M. Karpie, Christopher T. Sachrajda, Amarjit Soni, and Bigeng Wang, Long-distance contribution to εK from lattice QCD, Phys. Rev. D **109,** 054501 (2024).

[20] G. Anzivino *et al.*, Workshop summary—Kaons@CERN 2023, Eur. Phys. J. C **84,** 377 (2024).

[21] Andrzej J. Buras, Kaon theory: 50 years later, arXiv:2307.15737.

[22] Evgueni Goudzovski *et al.*, Weak decays of strange and light quarks, arXiv:2209.07156.

[23] V. Bertone *et al.* (ETM Collaboration), Kaon mixing beyond the SM from $N_f = 2$ tmQCD and model independent constraints from the UTA, J. High Energy Phys. 03 (2013) 089; 07 (2013) 143(E).

[24] Laurent Lellouch, Flavor physics and lattice quantum chromodynamics, in *Les Houches Summer School: Session 93: Modern Perspectives in Lattice QCD: Quantum Field Theory and High Performance Computing* (2011), pp. 629–698, arXiv:1104.5484.

[25] C. R. Allton, L. Conti, A. Donini, V. Gimenez, Leonardo Giusti, G. Martinelli, M. Talevi, and A. Vladikas, B parameters for $\Delta S = 2$ supersymmetric operators, Phys. Lett. B **453,** 30 (1999).

[26] A. Donini, V. Gimenez, Leonardo Giusti, and G. Martinelli, Renormalization group invariant matrix elements of $\Delta S = 2$ and $\Delta I = 3/2$ four-fermion operators without quark masses, Phys. Lett. B **470,** 233 (1999).

[27] Ronald Babich, Nicolas Garron, Christian Hoelbling, Joseph Howard, Laurent Lellouch, and Claudio Rebbi, $\bar{K}^0$ mixing beyond the standard model and *CP*-violating electroweak penguins in quenched QCD with exact chiral symmetry, Phys. Rev. D **74,** 073009 (2006).

[28] P. A. Boyle, N. Garron, and R. J. Hudspith (RBC, UKQCD Collaborations), Neutral kaon mixing beyond the standard model with $N_f = 2 + 1$ chiral fermions, Phys. Rev. D **86,** 054028 (2012).

[29] Nicolas Garron, Renwick J. Hudspith, and Andrew T. Lytle (RBC/UKQCD Collaborations), Neutral kaon mixing beyond the standard model with $N_f = 2 + 1$ chiral fermions part 1: Bare matrix elements and physical results, J. High Energy Phys. 11 (2016) 001.

[30] Jaehoon Leem *et al.* (SWME Collaboration), Calculation of BSM kaon B-parameters using staggered quarks, Proc. Sci. LATTICE2014 (**2014**) 370 [arXiv:1411.1501].

[31] J. Tobias Tsang and Michele Della Morte, B-physics from lattice gauge theory, Eur. Phys. J. Special Topics **233,** 253 (2024).

[32] Peter A. Boyle, Luigi Del Debbio, Andreas Juttner, Ava Khamseh, Francesco Sanfilippo, and Justus Tobias Tsang, The decay constants f_D and f_{D_s} in the continuum limit of N_f=2+1 domain wall lattice QCD, J. High Energy Phys. 12 (2017) 008.

[33] Peter A. Boyle, Nicolas Garron, Renwick J. Hudspith, Christoph Lehner, and Andrew T. Lytle (RBC, UKQCD Collaborations), Neutral kaon mixing beyond the standard model with $n_f = 2 + 1$ chiral fermions. Part 2: Non perturbative renormalization of the $\Delta F = 2$ four-quark operators, J. High Energy Phys. 10 (2017) 054.

[34] Peter Boyle, Nicolas Garron, Julia Kettle, Ava Khamseh, and Justus Tobias Tsang, BSM kaon mixing at the physical point, EPJ Web Conf. **175,** 13010 (2018).

[35] Peter Boyle, Nicolas Garron, Renwick James Hudspith, Andreas Juttner, Julia Kettle, Ava Khamseh, and Justus

Tobias Tsang, Beyond the standard model kaon mixing with physical masses, Proc. Sci. LATTICE2018 (**2019**) 285 [arXiv:1812.04981].

[36] A. Nicholson *et al.*, Heavy physics contributions to neutrinoless double beta decay from QCD, Phys. Rev. Lett. **121**, 172501 (2018).

[37] William Detmold, William I. Jay, David J. Murphy, Patrick R. Oare, and Phiala E. Shanahan, Neutrinoless double beta decay from lattice QCD: The short-distance $\pi^- \to \pi^+ e^- e^-$ amplitude, Phys. Rev. D **107**, 094501 (2023).

[38] F. Gabbiani, E. Gabrielli, A. Masiero, and L. Silvestrini, A complete analysis of FCNC and *CP* constraints in general SUSY extensions of the standard model, Nucl. Phys. **B477**, 321 (1996).

[39] Taegil Bae *et al.* (SWME Collaboration), Neutral kaon mixing from new physics: Matrix elements in $N_f = 2 + 1$ lattice QCD, Phys. Rev. D **88**, 071503 (2013).

[40] Damir Becirevic and Giovanni Villadoro, Remarks on the hadronic matrix elements relevant to the SUSY $K^0 - \bar{K}^0$ mixing amplitude, Phys. Rev. D **70**, 094036 (2004).

[41] C. Allton *et al.* (RBC-UKQCD Collaborations), Physical results from $2 + 1$ flavor domain wall QCD and SU(2) chiral perturbation theory, Phys. Rev. D **78**, 114509 (2008).

[42] Y. Aoki *et al.* (RBC, UKQCD Collaborations), Continuum limit physics from $2 + 1$ flavor domain wall QCD, Phys. Rev. D **83**, 074508 (2011).

[43] Peter A. Boyle, Luigi Del Debbio, Nicolas Garron, Andreas Juttner, Amarjit Soni, Justus Tobias Tsang, and Oliver Witzel (RBC/UKQCD Collaborations), SU(3)-breaking ratios for $D_{(s)}$ and $B_{(s)}$ mesons, arXiv:1812.08791.

[44] Y. Iwasaki and T. Yoshie, Renormalization group improved action for SU(3) lattice gauge theory and the string tension, Phys. Lett. **143B**, 449 (1984).

[45] Y. Iwasaki, Renormalization group analysis of lattice theories and improved lattice action: Two-dimensional nonlinear O(N) sigma model, Nucl. Phys. **B258**, 141 (1985).

[46] Richard C. Brower, Hartmut Neff, and Kostas Orginos, Mobius fermions: Improved domain wall chiral fermions, Nucl. Phys. B, Proc. Suppl. **140**, 686 (2005).

[47] R. C. Brower, H. Neff, and K. Orginos, Mobius fermions, Nucl. Phys. B, Proc. Suppl. **153**, 191 (2006).

[48] Richard C. Brower, Harmut Neff, and Kostas Orginos, The Möbius domain wall fermion algorithm, Comput. Phys. Commun. **220**, 1 (2017).

[49] Yigal Shamir, Chiral fermions from lattice boundaries, Nucl. Phys. **B406**, 90 (1993).

[50] Peter A. Boyle, Guido Cossu, Azusa Yamaguchi, and Antonin Portelli, GRID: A next generation data parallel C++ QCD library, Proc. Sci. LATTICE2015 (**2016**) 023.

[51] Azusa Yamaguchi, Peter Boyle, Guido Cossu, Gianluca Filaci, Christoph Lehner, and Antonin Portelli, GRID: OneCode and FourAPIs, Proc. Sci. LATTICE2021 (**2022**) 035 [arXiv:2203.06777].

[52] Antonin Portelli *et al.*, aportelli/hadrons: Hadrons v1.4 (2023).

[53] M. Foster and Christopher Michael (UKQCD Collaboration), Quark mass dependence of hadron masses from lattice QCD, Phys. Rev. D **59**, 074503 (1999).

[54] C. McNeile and Christopher Michael (UKQCD Collaboration), Decay width of light quark hybrid meson from the lattice, Phys. Rev. D **73**, 074506 (2006).

[55] P. A. Boyle, A. Jüttner, C. Kelly, and R. D. Kenway, Use of stochastic sources for the lattice determination of light quark physics, J. High Energy Phys. 08 (2008) 086.

[56] Petros Dimopoulos, Gregorio Herdoíza, Mauro Papinutto, Carlos Pena, David Preti, and Anastasioss Vladikas (AL-PHA Collaboration), Non-perturbative renormalisation and running of BSM four-quark operators in $N_f = 2$ QCD, Eur. Phys. J. C **78**, 579 (2018).

[57] G. Martinelli, C. Pittori, Christopher T. Sachrajda, M. Testa, and A. Vladikas, A general method for nonperturbative renormalization of lattice operators, Nucl. Phys. **B445**, 81 (1995).

[58] C. Sturm, Y. Aoki, N. H. Christ, T. Izubuchi, C. T. C. Sachrajda *et al.*, Renormalization of quark bilinear operators in a momentum-subtraction scheme with a nonexceptional subtraction point, Phys. Rev. D **80**, 014501 (2009).

[59] R. Arthur and P. A. Boyle (RBC, UKQCD Collaborations), Step scaling with off-shell renormalisation, Phys. Rev. D **83**, 114511 (2011).

[60] R. Arthur, P. A. Boyle, N. Garron, C. Kelly, and A. T. Lytle (RBC, UKQCD Collaborations), Opening the Rome-Southampton window for operator mixing matrices, Phys. Rev. D **85**, 014501 (2012).

[61] P. A. Boyle, N. Garron, and A. T. Lytle (RBC-UKQCD Collaborations), Non-perturbative running and renormalization of kaon four-quark operators with $N_f = 2 + 1$ domain-wall fermions, Proc. Sci. LATTICE2011 (**2011**) 227 [arXiv:1112.0537].

[62] R. L. Workman *et al.* (Particle Data Group), Review of particle physics, Prog. Theor. Exp. Phys. **2022**, 083C01 (2022).

[63] Damir Becirevic and Giovanni Villadoro, Impact of the finite volume effects on the chiral behavior of f(K) and B(K). Phys. Rev. D **69**, 054010 (2004).

[64] C. Alexandrou *et al.* (Extended Twisted Mass Collaboration), Quark masses using twisted-mass fermion gauge ensembles, Phys. Rev. D **104**, 074515 (2021).

[65] A. Bazavov *et al.* (Fermilab Lattice, MILC, TUMQCD Collaborations), Up-, down-, strange-, charm-, and bottom-quark masses from four-flavor lattice QCD, Phys. Rev. D **98**, 054517 (2018).

[66] N. Carrasco *et al.* (European Twisted Mass Collaboration), Up, down, strange and charm quark masses with $N_f = 2 + 1 + 1$ twisted mass lattice QCD, Nucl. Phys. **B887**, 19 (2014).

[67] D. Giusti, V. Lubicz, C. Tarantino, G. Martinelli, F. Sanfilippo, S. Simula, and N. Tantalo, Leading isospin-breaking corrections to pion, kaon and charmed-meson masses with twisted-mass fermions, Phys. Rev. D **95**, 114504 (2017).

[68] A. T. Lytle, C. T. H. Davies, D. Hatton, G. P. Lepage, and C. Sturm (HPQCD Collaboration), Determination of quark masses from n_f=4 lattice QCD and the RI-SMOM intermediate scheme, Phys. Rev. D **98**, 014513 (2018).

[69] Bipasha Chakraborty, C. T. H. Davies, B. Galloway, P. Knecht, J. Koponen, G. C. Donald, R. J. Dowdall, G. P. Lepage, and C. McNeile, High-precision quark masses and

QCD coupling from $n_f = 4$ lattice QCD, Phys. Rev. D **91,** 054508 (2015).

[70] Mattia Bruno, Isabel Campos, Patrick Fritzsch, Jonna Koponen, Carlos Pena, David Preti, Alberto Ramos, and Anastassios Vladikas (ALPHA Collaboration), Light quark masses in $N_f = 2 + 1$ lattice QCD with Wilson fermions, Eur. Phys. J. C **80,** 169 (2020).

[71] S. Durr, Z. Fodor, C. Hoelbling, S. D. Katz, S. Krieg, T. Kurth, L. Lellouch, T. Lippert, K. K. Szabo, and G. Vulvert, Lattice QCD at the physical point: Simulation and analysis details, J. High Energy Phys. 08 (2011) 148.

[72] S. Durr, Z. Fodor, C. Hoelbling, S. D. Katz, S. Krieg, T. Kurth, L. Lellouch, T. Lippert, K. K. Szabo, and G. Vulvert, lattice QCD at the physical point: Light quark masses, Phys. Lett. B **701,** 265 (2011).

[73] A. Bazavov *et al.*, Staggered chiral perturbation theory in the two-flavor case and SU(2) analysis of the MILC data, Proc. Sci. LATTICE2010 (**2010**) 083 [arXiv:1011.1792].

[74] M. Bruno, I. Campos, J. Koponen, Carlos Pena, David Preti, Alberto Ramos, and Anastassios Vladikas (ALPHA Collaboration), Light and strange quark masses from $N_f = 2 + 1$ simulations with Wilson fermions, Proc. Sci. LATTICE2018 (**2019**) 220 [arXiv:1903.04094].

[75] A. Bazavov *et al.* (MILC Collaboration), MILC results for light pseudoscalars, Proc. Sci. CD09 (**2009**) 007 [arXiv: 0910.2966].

[76] C. McNeile, C. T. H. Davies, E. Follana, K. Hornbostel, and G. P. Lepage, High-precision c and b masses, and QCD coupling from current-current correlators in lattice and continuum QCD, Phys. Rev. D **82,** 034512 (2010).

[77] S. Durr *et al.* (BMW Collaboration), Precision computation of the kaon bag parameter, Phys. Lett. B **705,** 477 (2011).

[78] Jack Laiho and Ruth S. Van de Water, Pseudoscalar decay constants, light-quark masses, and B_K from mixed-action lattice QCD, Proc. Sci. LATTICE2011 (**2011**) 293 [arXiv: 1112.4861].

[79] Andrzej J. Buras, Jean-Marc Gérard, and William A. Bardeen, Large N approach to kaon decays and mixing 28 years later: $\Delta I = 1/2$ rule, $\hat{B}_K$ and ΔM_K, Eur. Phys. J. C **74,** 2871 (2014).

[80] Andrzej J. Buras and Jean-Marc Gérard, Dual QCD insight into BSM hadronic matrix elements for $K^0 - \bar{K}^0$ mixing from lattice QCD, Acta Phys. Pol. B **50,** 121 (2019).

[81] Justus Tobias Tsang, Neutral meson mixing in the $B^0_{(s)}$ sector from lattice QCD, Proc. Sci. CKM2021 (**2023**) 107 [arXiv:2204.01259].

[82] Peter Boyle, Felix Erben, Andreas Jüttner, Takashi Kaneko, Michael Marshall, Antonin Portelli, Oliver Witzel, Luigi Del Debbio, and Justus Tobias Tsang, BSM $B - \bar{B}$ mixing on JLQCD and RBC/UKQCD $N_f = 2 + 1$ DWF ensembles, Proc. Sci. LATTICE2021 (**2022**) 224 [arXiv:2111.11287].

[83] www.dirac.ac.uk.

[84] Y. Aoki *et al.* (RBC, UKQCD Collaborations), Continuum limit physics from $2 + 1$ flavor domain wall QCD, Phys. Rev. D **83,** 074508 (2011).

[85] C. Urbach, K. Jansen, A. Shindler, and U. Wenger, HMC algorithm with multiple time scale integration and mass preconditioning, Comput. Phys. Commun. **174,** 87 (2006).

[86] Yu-Chih Chen and Ting-Wai Chiu (TWQCD Collaboration), Exact pseudofermion action for Monte Carlo simulation of domain-wall fermion, Phys. Lett. B **738,** 55 (2014).

[87] C. Jung, C. Kelly, R. D. Mawhinney, and D. J. Murphy, Domain wall fermion QCD with the exact one flavor algorithm, Phys. Rev. D **97,** 054503 (2018).

[88] M. A. Clark, Balint Joo, A. D. Kennedy, and P. J. Silva, Improving dynamical lattice QCD simulations through integrator tuning using Poisson brackets and a force-gradient integrator, Phys. Rev. D **84,** 071502 (2011).

[89] Hantao Yin and Robert D. Mawhinney, Improving DWF simulations: The force gradient integrator and the Möbius accelerated DWF solver, Proc. Sci. LATTICE2011 (**2011**) 051 [arXiv:1111.5059].

[90] Martin Lüscher, Stochastic locality and master-field simulations of very large lattices, EPJ Web Conf. **175,** 01002 (2018).

[91] Mattia Bruno, Marco Cè, Anthony Francis, Patrick Fritzsch, Jeremy R. Green, Maxwell T. Hansen, and Antonio Rago, Exploiting stochastic locality in lattice QCD: Hadronic observables and their uncertainties, J. High Energy Phys. 11 (2023) 167.

[92] Markus Fierz, Zur Fermischen Theorie des β-Zerfalls, Z. Phys. **104,** 553 (1937).

[93] Nicolas Garron, Fierz transformations and renormalization schemes for fourquark operators, EPJ Web Conf. **175,** 10005 (2018).

[94] Y. Aoki, P. A. Boyle, N. H. Christ, C. Dawson, M. A. Donnellan *et al.*, Non-perturbative renormalization of quark bilinear operators and B(K) using domain wall fermions, Phys. Rev. D **78,** 054510 (2008).

[95] Peter Boyle, Luigi Del Debbio, and Ava Khamseh, Massive momentum-subtraction scheme, Phys. Rev. D **95,** 054505 (2017).

[96] Luigi Del Debbio, Felix Erben, Jonathan Flynn, Rajnandini Mukherjee, and J. Tobias Tsang, Charm quark mass using a massive nonperturbative renormalisation scheme, Proc. Sci. LATTICE2023 (**2024**) 294 [arXiv:2312 .16537].

[97] Nicolas Garron, Caroline Cahill, Martin Gorbahn, J. A. Gracey, and P. E. L. Rakow, Exploring interpolating momentum schemes, Proc. Sci. LATTICE2021 (**2022**) 438 [arXiv:2202.04394].

[98] See Supplemental Material at http://link.aps.org/ supplemental/10.1103/PhysRevD.110.034501 for *Mathematica*, Version 14.0 (Wolfram Research Inc., Champaign, IL, 2024).

[99] Marco Ciuchini, E. Franco, V. Lubicz, G. Martinelli, I. Scimemi, and L. Silvestrini, Next-to-leading order QCD corrections to $\Delta F = 2$ effective Hamiltonians, Nucl. Phys. **B523,** 501 (1998).

[100] Andrzej J. Buras, Mikolaj Misiak, and Jorg Urban, Two loop QCD anomalous dimensions of flavor changing four quark operators within and beyond the standard model, Nucl. Phys. **B586,** 397 (2000).

[101] Andrzej J. Buras, Sebastian Jager, and Jorg Urban, Master formulae for $\Delta F = 2$ NLO QCD factors in the standard model and beyond, Nucl. Phys. **B605,** 600 (2001).

[102] Mauro Papinutto, Carlos Pena, and David Preti, On the perturbative renormalization of four-quark operators for

new physics, Eur. Phys. J. C **77,** 376 (2017); **78,** 21(E) (2018).

[103] P. A. Baikov, K. G. Chetyrkin, and J. H. Kühn, Five-loop running of the QCD coupling constant, Phys. Rev. Lett. **118,** 082002 (2017).

[104] F. Herzog, B. Ruijl, T. Ueda, J. A. M. Vermaseren, and A. Vogt, The five-loop beta function of Yang-Mills theory with fermions, J. High Energy Phys. 02 (2017) 090.

[105] Thomas Luthe, Andreas Maier, Peter Marquard, and York Schroder, Complete renormalization of QCD at five loops, J. High Energy Phys. 03 (2017) 020.

[106] K. G. Chetyrkin, Johann H. Kuhn, and Christian Sturm, QCD decoupling at four loops, Nucl. Phys. **B744,** 121 (2006).

[107] Y. Schroder and M. Steinhauser, Four-loop decoupling relations for the strong coupling, J. High Energy Phys. 01 (2006) 051.

[108] Tao Liu and Matthias Steinhauser, Decoupling of heavy quarks at four loops and effective Higgs-fermion coupling, Phys. Lett. B **746,** 330 (2015).

[109] K. G. Chetyrkin, Johann H. Kuhn, and M. Steinhauser, RunDec: A *Mathematica* package for running and

decoupling of the strong coupling and quark masses, Comput. Phys. Commun. **133,** 43 (2000).

[110] Barbara Schmidt and Matthias Steinhauser, CRunDec: A C++ package for running and decoupling of the strong coupling and quark masses, Comput. Phys. Commun. **183,** 1845 (2012).

[111] Florian Herren and Matthias Steinhauser, Version 3 of RunDec and CRunDec, Comput. Phys. Commun. **224,** 333 (2018).

[112] P. A. Baikov, K. G. Chetyrkin, and J. H. Kühn, Quark mass and field anomalous dimensions to $\mathcal{O}(\alpha_s^5)$, J. High Energy Phys. 10 (2014) 076.

[113] Thomas Luthe, Andreas Maier, Peter Marquard, and York Schröder, Five-loop quark mass and field anomalous dimensions for a general gauge group, J. High Energy Phys. 01 (2017) 081.

[114] P. A. Baikov, K. G. Chetyrkin, and J. H. Kühn, Five-loop fermion anomalous dimension for a general gauge group from four-loop massless propagators, J. High Energy Phys. 04 (2017) 119.

[115] S. Aoki *et al.* (Flavour Lattice Averaging Group), FLAG review 2019: Flavour Lattice Averaging Group (FLAG), Eur. Phys. J. C **80,** 113 (2020).